Atmospheric
Chemistry
and Physics
Discussions

Open Access

EGU

1 **Investigating the role of dust in ice nucleation within clouds and**

2 **further effects on the regional weather system over East Asia**

3 **Part II: modification of the weather system**

4 Lin Su[1], and Jimmy C.H. Fung[2,3]

5 [1] School of Science, Hong Kong University of Science and Technology, Hong Kong, China

6 [2] Division of Environment, Hong Kong University of Science and Technology, Hong Kong, China

7 [3] Department of Mathematics, Hong Kong University of Science and Technology, Hong Kong, China

8 *Correspondence to: Lin Su (lsu@connect.ust.hk)*

9

10 **Keywords:** East Asian dust; radiative forcing; clouds; precipitation; regional modeling

11

12 **Highlights:**

13 The semi-direct and indirect effects of dust are more pronounced than the direct effect on the regional weather

14 system.

15 The semi-direct and indirect effects of dust result in an increase in mid- to high clouds, and a reduction in low

16 clouds.

17 The total precipitation is reduced over most of China, but increased over South China by up to 20% or more.

Atmospheric
Chemistry
and Physics
Discussions

18   **Abstract.** An updated version of the Weather Research and Forecast model coupled with Chemistry (WRF-Chem)

19   was applied to quantify and discuss the full effects of dust on the meteorological field over East Asia during March

20   and April 2012. The performances of the model in simulating the short-wave and long-wave radiation, surface

21   temperature, and precipitation over East Asia are improved by incorporating the effects of dust in the simulations. The

22   radiative forcing induced by the dust-enhanced cloud radiative effect is over one order of magnitude larger than that

23   induced by the direct effect of dust. The semi-direct and indirect effects of dust result in a substantial increase in mid-

24   to high clouds, and a significant reduction in low clouds, leading to a decrease of near-surface temperature and an

25   increase of temperature at the mid- to upper troposphere over East Asia. The spatial redistribution of atmospheric

26   water vapor and modification of the vertical temperature profile over East Asia lead to an inhibition of atmospheric

27   instability over most land areas, but an enhancement of atmospheric instability over South China and the ocean,

28   resulting in a significant inhibition of convective precipitation in areas from central to East China, and a substantial

29   enhancement of convective precipitation over South China. Meanwhile, non-convective precipitation is also reduced

30   significantly over East Asia, as cloud droplets are hindered from growing large enough to form rain droplets, due to

31   the semi-direct and indirect effects of dust. The total precipitation can be reduced or increased by up to 20% or more.

32

1 Introduction

Dust is recognized as an "essential climate variable" because it is a major component of atmospheric aerosols and has significant impacts on the weather and climate system (Solomon, 2007). East Asian dust is an important contributor to global dust emissions (Ginoux et al., 2001), and thus play a significant role in affecting the regional weather system through direct effect, semi-direct and indirect effects.

Dust particles affect the radiation budget directly by absorbing, reflecting and scattering short-wave and long-wave radiation (Satheesh et al., 2006;Seinfeld et al., 2004;Lacis, 1995). The cloud radiative effect induced by dust is referred to as the semi-direct effect of dust. Dust particles within clouds can absorb radiation and heat up the surrounding environment, leading to faster evaporation rate of cloud droplets and thus a reduction of cloud cover. The indirect effects of dust are related to dust–cloud–interaction. (Hansen et al., 1997;Perlwitz and Miller, 2010). Dust particles are recognized as effective ice nuclei and considered to play an important role in cold cloud processes. Dust particles can significantly influence the ice water content in mixed-phase and ice clouds, and affect the formation and development of clouds, as well as precipitations (Sassen et al., 2003;Targino et al., 2006;Teller and Levin, 2006;Lohmann and Feichter, 2005).

In light of the significance of dust for the weather and climate system, assessing its effects of dust has become increasingly important. Many observational and modeling studies have aimed to quantify the various effects of dust. Due to the limited spatial and temporal availability of observational data, numerical modeling has proven an effective way to assess the effects of dust on the weather and climate system. The direct radiative effect of dust worldwide has being extensively studied using numerical methods (Mallet et al., 2009;Nabat et al., 2015a;Ge et al., 2010;Hartmann et al., 2013;Huang et al., 2009;Bi et al., 2013;Liu et al., 2011a;Liu et al., 2011b;Palacios et al., 2015;Huang, 2017). Recently, several studies have investigated the semi-direct effect of dust over different regions using various global and regional models (Tesfaye et al., 2015;Nabat et al., 2015b;Seigel et al., 2013). Unfortunately, due to the poor understanding of the dust–cloud–interaction in microphysical processes, quantifying the microphysical effect of dust remains as a difficult problem. Various ice nucleation parameterizations have been implemented into global models to estimate the importance of dust in atmospheric ice nucleation (Lohmann and Diehl, 2006;Karydis et al., 2011;Hoose et al., 2008;Zhang et al., 2014), revealing that the effect of dust as ice nuclei should not be neglected in numerical models, especially in the simulations over arid regions during strong wind events (DeMott et al., 2003;Koehler et al.,

Atmospheric
Chemistry
and Physics
Discussions

60   2010;DeMott et al., 2015;Lohmann and Diehl, 2006;Atkinson et al., 2013). However, very rare work has been done

61   to investigate the indirect effects of dust on the regional weather system, especially over East Asia, which is one of

62   the major contributors to the global dust emission in the world (Ginoux et al., 2001).

63   In this work, by applying an updated version of WRF-Chem, we aim to investigate the full effects of dust, including

64   the direct, the semi-direct, and the indirect effect, on the regional weather system over East Asia during a dust-intensive

65   period. In the updated WRF-Chem, The Goddard Chemistry Aerosol Radiation and Transport (GOCART) model has

66   been coupled with the aerosol-aware Thompson microphysics scheme, enabling the model to estimate the indirect

67   effect of dust along with the direct and semi-direct effects. This is the second part of a series of studies on the role of

68   East Asian dust in affecting the regional weather system, and also the first study to document the full effects of dust

69   during a typical dust-intensive period over East Asia by applying an online-coupled regional numerical model.

70   The remainder of the manuscript is organized as follows. The model configurations is described in Section 2, followed

71   by the model validation in Section 3. The results along with the discussion will be presented in section 4, followed by

72   the concluding remarks in Section 5.

73

2 Model configurations

75   The simulations were performed using an updated version of WRF-Chem based on version 3.8.1 (Grell et al., 2016).

76   The GOCART-Thompson, which is the coupling of the GOCART aerosol model and the aerosol-aware Thompson

77   microphysics scheme, has been implemented in the updated WRF-Chem, to evaluate the indirect effect of dust on the

78   atmospheric ice nucleation process by serving as ice nuclei. The implementation of GOCART-Thompson

79   microphysics scheme was described in detail in the first part of this study. According to the results of the sensitivity

80   experiments in Part I, the calibration factor cf is set to be 4, and the threshold relative humidity is set to be 100% in

81   the ice nucleation parameterization for the simulations run with dust emissions in this study.

82   Four numerical simulations were carried out to evaluate the separate effects of dust over East Asia. The configurations

83   for the four simulations are summarized in Table 1. The first simulation was termed NO-AER/NO-CLOUD, and was

84   conducted without dust, with both the aerosol radiative feedback and cloud radiative feedback turned off. The second

85   simulation, NO-AER/CLOUD, was also conducted without dust, with the aerosol radiative feedback turned off, but

86   the cloud radiative feedback turned on to estimate the intrinsic radiative effect of cloud. The third simulation,

Atmospheric
Chemistry
and Physics
Discussions

Open Access

EGU

87   AER/NO-CLOUD, was conducted with the presence of dust, with the aerosol radiative feedback turned on, while the

88   cloud radiative feedback still turned off. The difference between NO-AER/NO-CLOUD and AER/NO-CLOUD

89   therefore represented the direct effect of dust on the radiation budget and other meteorological parameters. The last

90   simulation, AER/CLOUD, was conducted with the presence of dust, and with both aerosol radiative feedback and

91   cloud radiative feedback turned on, to estimate the full effect of dust on the meteorological field over East Asia

92   The important physical and chemical parameterization schemes applied for the simulations are summarized and shown

93   in Table 1. The GOCART aerosol model was applied to simulate the aerosol processes (Ginoux et al., 2001;Ginoux

94   et al., 2004). For the dust emission simulation in AER/NO-CLOUD and AER/CLOUD, the Shao's dust emission

95   scheme was applied, which had been demonstrated to closly reproduced the dust emissions over East Asia. The

96   Mellor–Yamada–Janjic (MYJ) turbulent kinetic energy scheme was used for the planetary boundary layer

97   parameterization (Janjić, 2002, 1994); the moisture convective processes were parameterized by the Grell–Freitas

98   scheme (Grell and Freitas, 2014); the short-wave (SW) and long-wave (LW) radiation budgets were calculated by the

99   Rapid Radiative Transfer Model for General Circulation (RRTMG) SW and LW radiation schemes (Mlawer et al.,

100   1997;Iacono et al., 2008); gravitational settling and surface deposition were combined for aerosol dry deposition

101   (Wesely, 1989); a simple washout method was used for the below-cloud wet deposition of aerosols; and the aerosol

102   optical properties were calculated based on the volume-averaging method. The newly-implemented wet scavenging

103   scheme described in Part I of this study was used for the in-cloud wet scavenging of dust particles caused by the

104   microphysical processes. The configurations for NO-AER/NO-CLOUD and NO-AER/CLOUD were mostly the same

105   as for the other two simulations, but without a dust emission scheme, aerosol dry and wet deposition schemes, and

106   aerosol optical schemes, as no dust is produced in these two simulations. Note that in the two NO-CLOUD simulations,

107   a default ice nuclei concentration of 1 per Liter is used for the heterogeneous ice nucleation process.

108   As described in the first part of this manuscript, two nested domains were used for all four simulations, the outer

109   domain had a horizontal resolution of 27 km, covering the entire East Asia region, and the inner domain had a

110   horizontal resolution of 9 km, covering the entire central to East China. Both domains have 40 layers, with the top

111   layer at 50 hPa. The simulation period was March 9 to April 30, 2012, with the first eight days as "spin-up" time. Only

112   the results from March 17 to April 30, 2012 were used for further analysis. Final reanalysis data provided by the

113   United States National Center of Environmental Prediction, with a horizontal resolution of 1°, were used for generating

114   the initial and boundary conditions for the meteorological field. The simulations were re-initialized every 4 days, with

Atmospheric
Chemistry
and Physics
Discussions

115   the aerosol field being recycled, i.e., the output of the aerosol field from the previous 4-day run was used as the initial

116   aerosol state for the next 4-day run.

117

118   **3 Model validation**

119   The simulation for dust emission was validated in Part I of this study, and the model was demonstrated to closely

120   reproduce dust emissions over East Asia during the investigated period by comparison with comprehensive

121   observational data. As this study focused on the modification of the meteorological field by the effects of dust over

122   East Asia, the capability of the model in simulating the meteorological field itself over this region requires further

123   validation.

124   The China meteorological forcing dataset (Yang et al., 2010;Chen et al., 2011) was used to assess the performance of

125   the model in reproducing the spatial distribution of the meteorological field over China. The dataset was developed

126   by the hydrometeorological research group at the Institute of Tibetan Plateau Research, Chinese Academy of Science,

127   by merging the Princeton meteorological forcing data (Sheffield et al., 2006), the Global Energy and Water Cycle

128   Experiment–Surface Radiation Budget (GEWEX-SRB) forcing data (Pinker and Laszlo, 1992), and the Global Land

129   Data Assimilation System forcing dataset (Rodell et al., 2004). The dataset contains gridded observations of the near-

130   surface temperature, precipitation rate, surface downward SW and LW radiation across China, with a spatial resolution

131   of 0.25°, dating from 1996.

132   As this study aimed to evaluate the radiative forcing induced by dust, it was necessary to verify the performance of

133   the model in reproducing the radiative budget. The spatial distributions for the monthly average observational SW and

134   LW radiation from the China meteorological forcing dataset, and the simulated SW and LW radiation over East Asia

135   from NO-AER/CLOUD and AER/CLOUD, are shown in Figures 1 and 2. Note that only simulation results from NO-

136   AER/CLOUD and AER/CLOUD are shown, as they represent the intrinsic meteorological field and the

137   meteorological field modified by the effects of dust, respectively. For March, the comparison is restricted to the

138   observational data from March 17 to March 31, 2012, to ensure temporal overlay with the corresponding simulation

139   period. No observational data over the ocean were available, so the simulated results over the ocean are also omitted

140   to simplify the comparison.

141   The spatial distributions for the monthly average observational downward surface SW radiation for March and April

142   2012 are shown in Figure 1a and b. Overall, the SW radiation was stronger in April than in March. The SW radiation

Atmospheric
Chemistry
and Physics
Discussions

Open Access
EGU

143   was significantly higher over the West and Northwest China, due to the higher elevation of terrain over these regions,

144   and lower over East and South China, due to the lower elevation and greater cloud coverage over those regions. The

145   model closely reproduced the spatial distributions of the SW radiation in both months and accurately captured the

146   trend from March to April in the simulation results from both NO-AER/CLOUD and AER/CLOUD, despite a certain

147   overestimation, especially over coastal areas of East and South China. This overestimation was likely due to the

148   underestimation of clouds by the model over these areas. Compared with inland areas, cloud coverage is always greater

149   over the coastal areas of East and South China due to the abundant water vapor. Therefore, the SW radiation budget

150   over coastal areas was more sensitive to the underestimation of clouds by the model. Nevertheless, a significant

151   improvement in the simulation of the SW radiation budget over East Asia can be seen in the results from AER/CLOUD

152   compared with those from NO-AER/CLOUD. Specifically, the SW radiation produced in AER/CLOUD (Figure 1e

153   and f) was significantly lower than that produced in NO-AER/CLOUD (Figure 1c and d) over China as a whole,

154   especially at the dust sources and surrounding areas over the north and northwest of the country, which is clearly more

155   consistent with the observations.

156   The spatial distributions for the monthly average observational downward surface LW radiation over China for March

157   and April 2012 are shown in Figure 2a and b. Two high-value areas can be observed. One is over Northwest China,

158   where the Taklimakan Desert is located. The strong downward LW radiation over this region was likely due to the

159   abundance of dust particles in the local atmosphere. Dust particles suspended in the atmosphere during dust events

160   can absorb SW radiation and heat the surrounding atmospheric layer, causing more LW radiation to be emitted

161   downward (and upward) by this layer. The other area of strong LW radiation was located over South China, which is

162   warmer and contains more atmospheric water vapor. Water vapor is a potent greenhouse gas, which efficiently absorbs

163   LW radiation emitted by the Earth and to heat the surrounding area, and thus increases the emission of LW radiation

164   downward (and upward) by the heated atmosphere. The model accurately simulated the spatial distributions of the

165   LW radiation over this region for both March and April in both NO-AER/CLOUD (Figure 2c and d) and AER/CLOUD

166   (Figure 2e and f), and indeed closely captured the spatial pattern of the LW radiation over China as a whole. The

167   difference between the results of NO-AER/CLOUD and AER/CLOUD in terms of LW radiation was not so significant

168   as that for SW radiation. However, the slightly higher LW radiation over the Gobi Desert produced by AER/CLOUD

169   (Figure 2e and f) was more consistent with the observations, indicating that the model reproduced the LW radiation

170   budget more accurately upon taking the effects of dust into account.

Atmospheric
Chemistry
and Physics
Discussions

171   The spatial distributions for the monthly average near-surface temperature over China from observed for March and

172   April 2012 are shown in Figure 3a and b. Similarly to the spatial distributions for the LW radiation, higher near-

173   surface temperatures were observed over Northwest China, which is a dry, arid area, and South China, which is closer

174   to the equator. The spatial distributions of the near-surface temperature over this region were well reproduced by the

175   model for both March and April in both NO-AER/CLOUD (Figure 3c and d) and AER/CLOUD (Figure 3e and f).

176   The model accurately captured the spatial pattern of the surface temperature, and the two simulations did not differ

177   significantly in their results.

178   The spatial distributions for the monthly average observational precipitation over China for March and April in 2012

179   are shown in Figure 4a and b. The precipitation increased from North to South China in both months, and increased

180   from March to April over the entire region. The spatial patterns of precipitation in March and April were mostly

181   reproduced by the model in both NO-AER/CLOUD (Figure 4c and d) and AER/CLOUD (Figure 4e and f), but the

182   model underestimated the precipitation in March in both simulations, especially over central and North China. In April,

183   the observed precipitation center was located over South China. Apart from underestimating the precipitation over

184   Central and North China, the NO-AER/CLOUD simulation predicted the precipitation center to be located in an area

185   spanning Hunan and Jiangxi (Figure 4d), which was to the north of the observed center, and it also significantly

186   underestimated the precipitation over South China compared with the observed values. In contrast, in the results of

187   AER/CLOUD (Figure 4f), the precipitation band from Hunan to Jiangxi was markedly weaker, while the precipitation

188   over South China was enhanced, which was clearly much more consistent with the observations.

189   The foregoing comparison of the simulation results with the observational data demonstrated that the model reasonably

190   reproducing the meteorological field over East Asia. Moreover, the meteorological field was produced more accurately

191   when the effects of dust were considered in the simulations, which consequently allows the dust-induced modification

192   of the meteorological field to be investigated.

193

194   **4 Results and discussion**

195   **4.1 Radiative effect**

196   The spatial distributions for the mean radiative forcing induced by dust at the top of the atmosphere, at the bottom of

197   the atmosphere, and within the atmosphere over East Asia during the simulation period are shown in Figures 6 and 7.

198   Note that all of the spatial distributions for radiative forcing shown in the two figures are the temporal mean over the

199   entire simulation period. The SW radiative forcing was calculated as follows.

200    $$SW_{TOA} = SWDOWN_{TOA} - SWUP_{TOA} \qquad (1)$$

201    $$SW_{BOT} = SWDOWN_{BOT} - SWUP_{BOT} \qquad (2)$$

202    $$SW_{ATM} = SW_{TOA} + SW_{BOT} \qquad (3)$$

203   where SW_{TOA} is the SW radiative forcing at the top of the atmosphere, and SW_{BOT} is the SW radiative forcing at the

204   bottom of the atmosphere, both with positive values representing downwelling radiation; SW_{ATM} is the radiative

205   forcing within the atmosphere, which is the sum of SW_{TOA} and SW_{BOT}, with positive values representing a net

206   warming effect within the atmosphere; $SWDOWN_{TOA}$ and $SWUP_{TOA}$ are the downwelling and upwelling SW

207   radiation at the top of the atmosphere, respectively; $SWUP_{BOT}$ and $SWDOWN_{BOT}$ are the upwelling and downwelling

208   SW radiation at the bottom of the atmosphere, respectively.

209   The LW radiative forcing was calculated as follows.

210    $$LW_{TOA} = -LWUP_{TOA} \qquad (4)$$

211    $$LW_{BOT} = LWDOWN_{BOT} - LWUP_{BOT} \qquad (5)$$

212    $$LW_{ATM} = LW_{TOA} + LW_{BOT} \qquad (6)$$

213   Where LW_{TOA} is the LW radiative forcing at the top of the atmosphere, and LW_{BOT} is the LW radiative forcing at the

214   bottom of the atmosphere, both with positive values representing downwelling radiation; LW_{ATM} is the radiative

215   forcing within the atmosphere, which is the sum of LW_{TOA} and LW_{BOT}, with positive values representing warming

216   effect within the atmosphere; $LWUP_{TOA}$ is the upwelling LW radiation at the top of the atmosphere; $LWUP_{BOT}$ and

217    $LWDOWN_{BOT}$ are the upwelling and downwelling LW radiation at the bottom of the atmosphere.

218   The net radiative forcing is the sum of SW and LW radiative forcing.

219    $$Ra_{TOA} = SW_{TOA} + LW_{TOA} \qquad (7)$$

220    $$Ra_{BOT} = SW_{BOT} + LW_{BOT} \qquad (8)$$

221    $$Ra_{ATM} = SW_{ATM} + LW_{ATM} \qquad (9)$$

222

223   **4.1.1 Clear-sky radiative forcing**

224   The direct radiative forcing induced by dust shown in Figure 5 is also referred to as clear-sky radiative forcing, and is

225   due to the reflection, absorption and emission of radiation by dust particles suspended in the atmosphere.

226   The clear-sky downwelling SW radiative forcing at the top of the atmosphere is slightly negative over most of East

Atmospheric
Chemistry
and Physics
Discussions

227   Asia (Figure 5a), indicating that the upwelling SW radiation at the top of the atmosphere increases due to the reflection

228   and scattering of SW radiation by dust particles. The clear-sky SW radiative forcing at the bottom of the atmosphere

229   is negative over most of East Asia (Figure 5g), especially over dust source regions, which suggests that the

230   downwelling SW radiation is significantly reduced through the absorption by dust particles suspended in the

231   atmosphere, leading to a significant net warming effect within the atmosphere (Figure 5d). Averaged over the entire

232   simulation domain, the SW radiative forcing over East Asia is -1.22 W/m^2 at the top of the atmosphere, -2.44 W/m^2

233   at the bottom of the atmosphere, and 1.23 W/m^2 within the atmosphere, accounting for 0.37%, 0.97%, and 1.58% of

234   the total clear-sky radiation budget in these three zones, respectively, as shown in Table 2.

235   In Figure 5b, the clear-sky downwelling LW radiation at the top of the atmosphere is slightly increased over dust

236   source regions and downwind areas, due to the absorption of LW radiation by the thick dust layer in the atmosphere.

237   In comparison, it is slightly reduced over other areas of East Asia, indicating an increase of the upwelling LW radiation,

238   which might be attributable to the greater emission of LW radiation by the dust layer, which in turn is due to the

239   heating of the atmosphere caused by the absorption of SW radiation by dust particles (Figure 5d). The clear-sky

240   downwelling LW radiation forcing is reduced at the bottom of the atmosphere (Figure 5h), which is attributed to the

241   Earth's surface being cooler as it receives less solar radiation (Figure 5g). Combining the LW radiative forcing at the

242   top of the atmosphere and at the bottom of the atmosphere, there is a net negative LW radiative forcing within the

243   atmosphere (Figure 5e). Overall, the mean LW radiative forcing averaged over the entire East Asia is relatively slight,

244   being -0.02 W/m^2 at the top of the atmosphere, 1.09 W/m^2 at the bottom of the atmosphere, and -1.07 W/m^2 within

245   the atmosphere, accounting for 0.01%, 1.18%, and 0.63% of the total clear-sky radiation budget in those three zones,

246   respectively.

247   Combining the SW and LW radiative forcing, the net downwelling clear-sky radiation at the top of the atmosphere is

248   reduced over most of East Asia (Figure 5c). The downwelling clear-sky net radiation at the bottom of the atmosphere

249   is reduced over most part of East Asia, especially over dust source regions and downstream areas (Figure 5i), leading

250   to a net warming effect within the atmosphere (Figure 5f), which is slightly smaller than the warming caused by SW

251   radiative forcing (Figure 5d). The net radiative forcing is -1.20 W/m^2 at the top of the atmosphere, -1.36 W/m^2 at the

252   bottom of the atmosphere, and 0.15 W/m^2 within the atmosphere, accounting for 1.78%, 0.85%, and 0.16% of the total

253   clear-sky radiation budget in those three zones.

254

4.1.2 All-sky radiative forcing

The all-sky radiative forcing induced by dust shown in Figure 6 is the total radiative forcing, including the radiative

forcing directly induced by dust displayed in Figure 5, and that induced by the cloud radiative effect enhanced by dust.

In Figure 6a, the all-sky downwelling SW radiation at the top of the atmosphere is markedly reduced over most of

China compared with the clear-sky case, due to greater reflection from dust and enhanced cloud cover induced by dust

over the continent. However, it is increased over the southern part of northwest Pacific, indicating less SW radiation

is reflected back into space due to the cloud radiative effect, which implies less cloud cover induced by dust over this

area. Compared with the clear-sky case, the all-sky upwelling SW radiation at the bottom of the atmosphere in Figure

6g is increased significantly over the continent, as more solar radiation is blocked due to the enhanced cloud cover

induced by dust; however, the downwelling all-sky SW radiation at the bottom of the atmosphere is reduced over most

of the West Pacific, indicating that more solar radiation that reaches the Earth's surface due to the cloud radiative

effect, which also implies less cloud cover over this area. The cloud radiative effect strengthens the warming within

the atmosphere over land in the all-sky case compared with the clear-sky case, while there is a slight cooling over the

ocean in the all-sky case, as shown in Figure 6d, in contrast to the slight warming in the clear-sky case. Averaged over

the entire simulation domain, the mean SW radiative forcing is -7.81 W/m^2 at the top of the atmosphere, and -7.87

W/m^2 at the bottom of the atmosphere (Table 2), accounting for 2.62% and 3.60% of the total all-sky radiation budget

in those two zones, respectively. Within the atmosphere, the positive SW radiative forcing over land and negative SW

radiative forcing over the ocean balance each other out.

Compared with the clear-sky case, the all-sky downwelling LW radiation at the top of the atmosphere is significantly

increased over almost the whole of East Asia (Figure 6b), indicating much less upwelling LW radiation at the top of

the atmosphere. The increase of downwelling all-sky LW radiation at the bottom of the atmosphere over land in Figure

6h is due to the greater emission of LW radiation by the warmer atmosphere, and the larger radiative forcing than that

in the clear-sky case implies that the cloud cover is significantly increased over land due to dust. Conversely, there is

no warming effect at the surface of the ocean, and the reduction in downwelling LW radiation over the ocean implies

less cloud cover over the ocean. The combination of the direct radiative effect of dust and the cloud radiative effect

enhanced by dust causes an overall increase of LW radiation within the atmosphere, leading to a warming effect,

which is more pronounced over the ocean, as shown in Figure 6e. The mean all-sky LW radiative forcing over the

entire simulation domain is 9.52 W/m^2 at the top of the atmosphere, accounting for 3.79% of the total all-sky LW

283   radiation budget in that zone. The increase of the all-sky LW radiation at the bottom of the at atmosphere over land

284   and its reduction over the ocean almost cancel each other out, leaving a mean all-sky LW radiation over the entire

285   simulation domain of 0.25W/m^2, accounting for 0.34% of the total LW radiation budget at the bottom of the

286   atmosphere. The mean all-sky LW radiative forcing within the atmosphere over the simulation domain is 9.26 W/m^2,

287   accounting for 5.25% of the total all-sky LW radiation budget within the atmosphere.

288   Summing the SW and LW radiative forcing, the net downwelling all-sky radiation at the top of the atmosphere is

289   reduced to the north of Central China, Korea, and Japan, and increased significantly over most of the ocean (Figure

290   6c). By contrast, the net doenwelling all-sky net radiation at the bottom of the atmosphere is reduced significantly

291   over the same land areas, and increased over most of the ocean (Figure 6i). Radiative forcing results in pronounced

292   warming within in the atmosphere over East Asia as a whole (Figure 6f). Averaged over the simulation domain, the

293   net all-sky radiative forcing is 1.70 W/m^2, -7.62 W/m^2, and 9.33 W/m^2 at the top of the atmosphere, at the bottom of

294   the atmosphere, and within the atmosphere, accounting for 3.61%, 5.28%, and 9.61% of the total net radiation budget

295   in those three zones, respectively.

296   In summary, the direct radiative effect of dust combined with the cloud radiative effect enhanced by dust causes a net

297   loss of radiation at the Earth's surface, but a net gain of radiation within the atmosphere, leading to a cooling at the

298   surface and lower troposphere, and a warming in mid- to upper troposphere. The radiative forcing caused by the dust-

299   enhanced cloud radiative effect is much greater than that caused by the direct radiative effect of dust, especially for

300   LW radiative forcing, which is highly affected by cloud cover. The LW radiative forcing caused by the dust-enhanced

301   cloud radiative effect is one order stronger than that cased by the direct radiative effect of dust at the top of the

302   atmosphere and within the atmosphere. The spatial distribution of radiative forcing further implies a shift of the spatial

303   distribution of cloud cover, such that the cloud cover is likely increased over land, but reduced over the ocean due to

304   the presence of dust, indicating a re-distribution of atmospheric water vapor over East Asia. The shift of the vertical

305   distribution of the radiation budget, the re-distribution of atmospheric water vapor, and the modification of

306   atmospheric stability resulting from those two processes will be discussed in more detail in later sections.

307

308   **4.2 Atmospheric water vapor**

309   **4.2.1 Spatial distribution**

310   The Semi-direct and indirect effects of dust particles lead to a modification of cloud format and cloud lifetime, and a

311   re-distribution of atmospheric water vapor. The spatial distributions of the simulated atmospheric water vapor path,

312   ice water path, and cloud water path from NO-AER/CLOUD and AER/CLOUD, as well as the difference

313   (AER/CLOUD − NO-AER/CLOUD) between the two simulations, are presented in Figure 7. The atmospheric water

314   vapor path, ice water path, and cloud water path are the column sums of water vapor, ice water vapor, and cloud water

315   vapor in the atmosphere per unit area. Note that the difference between NO-AER/CLOUD and AER/CLOUD is

316   entirely due to the combined effects of dust, i.e., the direct effect of dust, the cloud radiative effect enhanced by dust,

317   and the microphysical effect of dust serving as ice nuclei in the atmosphere. The spatial distributions shown in Figure

318   7 are the mean atmospheric water vapor path, ice water path, and cloud water path averaged over the whole simulation

319   period.

320   Figure 7a and b show the spatial distributions of precipitable water vapor in the atmosphere, which is equal to the total

321   volume of the atmospheric water path in the atmospheric column, over East Asia produced from NO-AER/CLOUD

322   and AER/CLOUD. The results from the two simulations are similar, with the same spatial pattern. The differences

323   between the two are shown in Figure 7c, in which the precipitable water vapor is slightly reduced by less than 1 mm

324   over most of East Asia, except for the dust source regions, over where the precipitable water vapor in the atmosphere

325   is slightly increased. However, the increase or reduction of precipitable water vapor induced by dust, which accounts

326   for less than 1% of the total amount of the precipitable water vapor in the atmosphere, is negligible.

327   The situation is different for the atmospheric ice water path. The atmospheric ice water path is lower than 1 g/m^2 over

328   most of East Asia in the results of NO-AER/CLOUD (Figure 7d), indicating that the production of ice crystals, or ice

329   clouds, in the atmosphere is rare in the simulation without dust. By contrast, the atmospheric ice water path produced

330   by AER/CLOUD is substantially higher than that produced by NO-AER/CLOUD over the entire simulation domain,

331   with values higher than 20 g/m^2 over much of East Asia (Figure 7e). This corresponding to an increase of one order

332   over vast areas, from dust source regions to the Northwest Pacific (Figure 7f), due to the dust particles serving as ice

333   nuclei in the atmosphere. Dust nuclei in the atmosphere enable the super-cooled water droplets to freeze into ice

334   crystals at a much higher temperature and lower relative humidity.

335   The spatial distribution for the mean atmospheric cloud water path over the entire simulation period from NO-

336   AER/CLOUD is shown in Figure 7g, in which the cloud water path is concentrated over South China and the West

337   Pacific, with values as high as 100 g/m^2. The spatial pattern of the atmospheric cloud water path from AER/CLOUD

338   in Figure 7h is qualitatively similar to that from NO-AER/CLOUD, but with much lower values. The comparison of

Atmospheric
Chemistry
and Physics
Discussions

339   atmospheric cloud water paths between AER/CLOUD and NO-AER/CLOUD in Figure 7i shows that the atmospheric

340   cloud water path is reduced by more than 30 g/m^2 over south China, which accounts for one third of the total

341   atmospheric cloud water vapor over this region in the results of NO-AER/CLOUD.

342   Figure 8 shows the spatial distributions for the mean simulated ice crystal number density and cloud droplet number

343   density produced by NO-AER/CLOUD and AER/CLOUD over East Asia during the entire simulation period, as well

344   as the difference between the results from the two simulations (AER/CLOUD − NO-AER/CLOUD). Similar to the

345   case in Figure 8, the simulated ice crystal number density increases substantially when the ice nucleation process is

346   enhanced by dust particles serving as ice nuclei. Compared with that produced by NO-AER/CLOUD (Figure 8a), the

347   ice crystal number density produced by AER/CLOUD (Figure 8b) is one order higher over the simulation domain as

348   a whole, and increased by as much as 6×10^8 $/m^2$ over north China and the south part of the ocean area. By contrast,

349   the simulated cloud droplet number density produced by AER/CLOUD (Figure 8e) is much lower than that produced

350   by NO-AER/CLOUD (Figure 8d). In AER/CLOUD, the effects of dust reduce the cloud droplet number density by

351   around one third over this region compared with NO-AER/CLOUD (Figure 8f).

352

353   **4.2.2 Vertical profile**

354   As the spatial distributions of the ice water path and cloud water path over East Asia are altered by the effects of dust,

355   the cloud ice mixing ratio and cloud water mixing ratio are also modified vertically. Figure 9 shows the vertical profiles

356   of the cloud ice and cloud water mixing ratios under the combined effects of dust. Note that the vertical profiles over

357   land, over the ocean, and over the entire simulation domain for East Asia are averaged across the whole simulation

358   period.

359   Due to the effects of dust, the cloud ice mixing ratio is increased at all altitudes from the near-surface layer to higher

360   than 15 km over the whole of East Asia, with two peaks located at 12 km and 6 km, as shown in Figure 9a. The smaller

361   peak at 6 km is due to the enhanced cloud ice mixing ratio over land. The cloud ice mixing ratio is uniformly increased

362   between 4 km and 13 km over land (Figure 9b), which results from the increase of ice nuclei served by the abundant

363   dust particles in the atmosphere. In contrast, the increase of the cloud ice mixing ratio over the ocean from 7 km to 15

364   km, with a significant peak located at 12 km (Figure 9c). The enhancement of cloud ice mixing ratio over the ocean

365   is much greater than over land, likely due to more water vapor over the ocean. As noted above, the enhancement of

366   the cloud ice mixing ratio over the ocean also occurs at a higher altitude (7 km to 15 km) than that over land. A

Atmospheric
Chemistry
and Physics
Discussions

367   possible cause of this difference is that only those particles fined enough to be lifted to high altitudes can be transported

368   as far as the open ocean of the West Pacific, whereas over land, more dust particles with larger sizes are suspended in

369   lower layers before settling down to the surface.

370   The vertical modification of the cloud water mixing ratio due to the effects of dust is fundamentally different from

371   that of cloud ice mixing ratio. Due to the effects of dust, the cloud water mixing ratio at low layers from the near-

372   surface to 3 km decreases over the whole of East Asia, with the average decrease peaking at around 1.5 km (Figure

373   9d). The overall decrease is dominated by the reduction in the cloud water mixing ratio over the ocean (Figure 9f).

374   The cloud water mixing ratio is also decreased over land at the same layers (Figure 9e), but by smaller magnitudes

375   compared with the decrease over the ocean. The vertical modification of the cloud water mixing ratio suggests that

376   the effects of dust is the significantly reduce low clouds over East Asia, especially over the ocean, where there is much

377   more abundant water vapor for cloud formation.

378   To summarize Section 4.2, the effects of dust result in a general increase of cloud ice and decrease of cloud water over

379   East Asia as a whole, whereby the increase in cloud ice is mainly concentrated at the mid- to upper troposphere, while

380   the decrease of cloud water mostly occurs in low clouds.

381   The increase in cloud formation at the mid- to upper troposphere is attributed to the indirect effect of dust. The

382   abundant ice nuclei in the atmosphere served by dust particles substantially increase the amount of ice crystals in

383   mixed-phase and ice clouds at these altitudes. In contrast, the decrease of low clouds is the result of two factors. One

384   is the warming within the atmosphere induced by the dust, leading to a much higher saturation pressure required for

385   atmospheric water vapor to form clouds, and a much faster evaporation rate of cloud droplets, which is due to the

386   cloud burning effect of dust. The other factor is that the super-cooled cloud droplets in the upper layers of the

387   troposphere freeze into ice crystals at a much higher temperature and lower relative humidity when dust particles serve

388   as ice nuclei in the atmosphere, leading to an increase of atmospheric ice water path. Given an approximately constant

389   total amount of water vapor in the atmosphere, the increased formation of ice crystals by the freezing of cloud droplets

390   results in a reduction in the amount of liquid cloud, and thus the atmospheric cloud water path, over East Asia as a

391   whole. The redistribution of atmospheric water vapor further strengthens the cloud radiative effect and modifies the

392   radiation budget over East Asia, as discussed in Section 4.1.2.

393

394   **4.3 Vertical temperature profile**

Atmospheric
Chemistry
and Physics
Discussions
Open Access
EGU

395   Due to the radiative forcing directly induced by dust discussed in Section 4.1.1, and the cloud radiative effect enhanced

396   by dust discussed in Section 4.1.2, the vertical temperature profile is modified. Figure 10 shows the modifications of

397   the vertical temperature profiles induced by the direct radiative effect of dust, the cloud radiative effect enhanced by

398   dust, and the full radiative effect of dust over the whole of East Asia, over land, and over the ocean during the

399   investigated period.

400   On average, the temperature over the simulation domain as a whole is slightly increased in the near-surface atmosphere,

401   decreased from 1 km to 3 km, increased significantly from 1 km up to 13 km, and then decreased above 13 km (Figure

402   10a). The contributions of the direct radiative effect of dust and dust-enhanced cloud radiative effect to the vertical

403   temperature modification are shown in Figure 10b and c. The direct radiative effect of dust (Figure 10b) results in a

404   decrease of temperature at the near-surface layer, and an increase above 1 km. In contrast, the pattern of the vertical

405   temperature modification caused by dust-enhanced cloud radiative effect (Figure 10c) is similar to that caused by the

406   full effect of dust, and is one order of magnitude larger magnitude than that caused by the direct radiative effect of

407   dust.

408   As the radiative forcing induced by dust over land differs from that over the ocean, the effects on the vertical

409   temperature profile requires further discussion. The decrease in temperature at the lower level of the troposphere

410   mainly occurs over land. The temperature over land decreases significantly below 2 km, then increases gradually from

411   2 km to 12 km, and decreases again over 12 km (Figure 10d). The decrease in temperature at the lower level is

412   composed of roughly equal contributions from the direct radiative effect and the dust-enhanced cloud radiative effect.

413   However, the increase in the temperature between 2 km and 12 km is mainly attributable to the dust-enhanced cloud

414   radiative effect (Figure 10f), the contribution of which is one order larger than that of the direct radiative effect of dust

415   (Figure 10e). The decrease in temperature at lower layers is mainly attributable to the negative SW radiative forcing

416   at the surface induced by dust, and the increase of temperature at the mid- to upper troposphere is due to the absorption

417   of LW radiation by dust-enhanced ice clouds.

418   The modification of the vertical temperature profile over the ocean is similar to that over East Asia as a whole,

419   especially at lower layers from the surface to 3 km, with an increase in temperature at the near-surface below 2 km,

420   and a decrease in temperature from 1 km to 3 km (Figure 10g). The direct radiative effect of dust results in a slight

421   decrease in temperature at the surface and at altitudes from 7 km to 9 km, but a slight increase from 1 km to 7 km and

422   above 10 km (Figure 10h). The dust-enhanced cloud radiative effect causes an overall increase in temperature from

423   the surface to 13 km, with a minor peak at an altitude of 1 km and a major peak at an altitude of 11 km (Figure 10i).

424   The modification of the vertical temperature profile over the ocean is mostly contributed by the dust-enhanced cloud

425   radiative effect over the ocean, with an almost identical pattern and magnitude to the temperature variation over East

426   Asia as a whole (Figure 10i).

427   The patterns of vertical temperature modification over land and ocean are due to different mechanisms. The vertical

428   temperature profile over land is chiefly modified by the direct radiative effect of dust at lower layers, and by the

429   enhanced cloud radiative effect due to the greater amount of ice clouds at the mid- to upper troposphere. With a heavier

430   dust burden over land, the SW radiation is blocked more effectively from reaching the land surface than the ocean

431   surface. Furthermore, the temperature at the near-surface layer over land responds to the SW radiation much faster

432   than that over the ocean, leading to a greater temperature decrease at lower levels over land. In the mid- to upper

433   troposphere, the greater amount of ice cloud leads to greater absorption of LW radiation emitted by the Earth, and the

434   enhanced freezing of cloud droplets into ice crystals promotes the release of latent heat, leading to a significant

435   increase of temperature in the surrounding atmosphere. The decrease in temperature below 2 km and the increase in

436   temperature above 2 km are likely to reduce atmospheric instability, which in turn will weakens the convective

437   motions over land.

438   The mechanism for the modification of the vertical temperature profile over the ocean is more complicated. As

439   discussed in Section 4.2, the effects of dust result in a substantial reduction of clouds, especially low clouds, and a

440   marked increase of ice clouds at the mid- to upper troposphere over the ocean. As ice clouds are much less efficient

441   in blocking solar radiation than low clouds, the reduction of low clouds leads to an increase of SW radiation over the

442   ocean, which heats up the ocean surface and near-surface layer of the atmosphere. Conversely, the reduction of low

443   clouds between 1 km and 3 km results in less LW radiation being absorbed by low clouds, and also less latent heat

444   being released by the condensation of water vapor into cloud droplets, both of which lead to a significant decrease of

445   temperature at layers between 1 km and 3 km. The increase in temperature above 3 km has the same cause as that over

446   land. The greater amount of ice clouds in the mid- to upper troposphere is able to absorb more of the LW radiation

447   emitted by the Earth, and the enhanced freezing of cloud droplets into ice crystals promotes the release of latent heat

448   into the surrounding atmosphere, leading to a significant increase in temperature in these layers. The cooling below 1

449   km and warming between 1 km and 3 km are likely to enhance atmospheric instability, causing stronger convective

450   motions over the ocean.

Atmospheric
Chemistry
and Physics
Discussions

451

4.4 Atmospheric stability

As discussed above, the radiative forcing and the re-distribution of atmospheric water content induced by dust result

in a modification of the vertical temperature profile over East Asia. The corresponding shift of the thermal energy in

the atmosphere eventually lead to a modification of the atmospheric stability over this region.

The K-index (KI) is a metric widely used in meteorology to evaluate atmospheric stability, and is calculated with the

following equation (George, 2014):

$$KI = T_{850} - T_{500} + Td_{850} - (T_{700} - Td_{700}) \qquad (10)$$

where T_{850}, T_{700}, and T_{500} are the respective temperatures at 850 hPa, 700 hPa, and 500 hPa, and Td_{850} and Td_{700}

are the dew points at 850 hPa and 700 hPa. The calculation of KI considers the atmospheric stability as a function of

the vertical temperature lapse rate, the moisture content of the lower atmosphere, and the vertical extent of the moist

layer. The larger the value of KI, the more unstable the atmosphere. To evaluate the effect of dust on atmospheric

stability, KI was calculated from the simulation outputs.

Figure 11 shows the spatial distributions for the mean KI from NO-AER/CLOUD over East Asia during the simulation

period, which represents the intrinsic average atmospheric stability free from the effects of dust, and Figure 12 shows

the spatial distributions for the mean difference in KI between AER/NO-CLOUD and NO-AER/NO-CLOUD (Figure

12a), between AER/CLOUD and NO-AER/CLOUD (Figure 12b), and between AER/CLOUD and NO-AER/ CLOUD

(Figure 12c). The differences represent the modification in KI induced by the direct radiative effect of dust in Figure

12a, semi-direct and indirect effects, including cloud radiative effects and re-distribution of atmospheric water content

enhanced by dust, in Figure 12b, and the combined effects of the previous two in Figure 12c.

As shown in Figure 11, the mean KI over East Asia is lower in the north and increases gradually from north to south,

with the highest values located over the South China Sea and Southeast Asia, and the lowest values over the Central

to North Pacific.

Under the full effects of dust, the mean modification of KI over most land areas in East Asia is a significant decrease.

The largest decrease occurs over the dust source regions and central to East China (Figure 12c), and results from the

vertical modification over land. In contrast, KI significantly increases over most areas of the ocean and South China,

due to the different effects of dust on the vertical temperature over these areas, as discussed in Section 4.3. The

contributions of the direct radiative effect of dust and the indirect effects of dust on the modification of the mean KI

Atmospheric
Chemistry
and Physics
Discussions

479   are shown in Figure 12a and b. The direct radiative effect of dust is to inhibit the atmospheric instability is inhibited

480   over most land areas, indicated by a significant decrease of the mean KI, as shown in Figure 12a. However, the overall

481   modification of mean KI is even greater over the ocean when the semi-direct and indirect effects of dust are taken into

482   account. Upon considering the semi-direct and indirect effects of dust, the modification of KI is much greater over

483   areas with more water vapor in the simulation domain, such as South China and most ocean areas, as shown in Figure

484   12b.

485   Overall, the atmosphere is significantly stabilized over the dust source regions and central to East China, but

486   significantly destabilized over South China and most ocean areas, due to the effects of dust. The dust-enhanced cloud

487   radiative forcing and the re-distribution of atmospheric water content due to dust contribute much more to the

488   modification of atmospheric stability than the direct radiative effect of dust does, especially over areas with abundant

489   water vapor.

490

491   **4.5 Precipitation**

492   The modification of atmospheric stability and re-distribution of atmospheric water content induced by dust eventually

493   alter the precipitation over East Asia. The spatial distributions for the mean precipitation rate, including total

494   precipitation, convective precipitation, and non-convective precipitation from NO-AER/CLOUD and AER/CLOUD,

495   as well as the difference between the two simulations, are shown in Figure 13. Note that the precipitation rate shown

496   in Figure 14 is the mean daily precipitation rate averaged over the simulation period.

497   The spatial pattern of the mean total precipitation rate from NO-AER/CLOUD shown in Figure 13a is generally similar

498   to that from AER/CLOUD shown in Figure 13b. However, as discussed in Section 3.2.2, the simulated precipitation

499   center produced in NO-AER/NO-CLOUD spans an area from Hunan to Jiangxi (Figure 13a), to the north of the

500   observed precipitation, and the simulated precipitation rate over South China is significantly lower than the

501   observational values. By contrast, in AER/CLOUD (Figure 13b), the precipitation band from Hunan to Jiangxi is

502   markedly inhibited, while the precipitation rate over South China is enhanced, which is clearly more consistent with

503   the observations. As shown in Figure 13c, the total precipitation is reduced by as much as 1 mm/day or more over

504   most land areas, but increased by up to 1 mm/day over South China, due to the effects of dust. The modifications in

505   precipitation account for over 20% of the total simulated precipitation rate over both land and the ocean.

506   The simulated convective precipitation mostly occurs over the southern part of the simulation domain, with

507 precipitation centers located over central to East China, South China, the South China Sea, and Southeast Asia (Figure

508 13d and e). The total precipitation over these areas is chiefly affected by the modification of convective precipitation.

509 Due to the effects of dust, convective precipitation is significantly reduced at the precipitation center from central to

510 East China, but substantially enhanced over South China and the ocean (Figure 13f). The inhibition of convective

511 precipitation over Central to East China has two reasons. One is the general enhancement of atmospheric stability,

512 which reduces the convective motion over this region. The other is the decrease in low clouds over South China and

513 the ocean, which reduces the availability of cloud droplets that can grow into rain droplets under the same

514 meteorological conditions. The greater convective precipitation over South China is due to the greater atmospheric

515 instability, which promotes convective motions.

516 The simulated non-convective precipitation is produced by the microphysics scheme. The Non-convective

517 precipitation mainly occurs at the western rim of the Taklimakan Desert, northeast China, Japan, and the areas between

518 27°N and 36°N over East Asia during the simulation period. The non-convective precipitation rate produced in

519 AER/CLOUD (Figure 13h) is markedly lower than that produced in NO-AER/CLOUD (Figure 13g) at the northern

520 precipitation centers. Figure 13i shows that the non-convective precipitation rate is reduced by more than 30% at the

521 western of the Taklimakan Desert and in the rain band from East China to Japan. More super-cooled water droplets

522 can freeze into ice crystals in the upper troposphere due to the abundant ice nuclei served by dust particles, leading to

523 much lower atmospheric cloud water content and cloud droplet number concentration directly above the non-

524 convective precipitation center. Furthermore, the warming within the atmosphere, which is caused by radiative forcing

525 and latent heat released by the freezing of super-cooled water droplets, results in a higher saturation pressure for water

526 vapor and faster evaporation rate for cloud droplets. This, in turn, suppresses the growth of cloud droplets into rain

527 droplets, leading to an inhibition of non-convective precipitation. Conversely, the increase in cloud ice in some cases

528 leads to more precipitation. The ice crystals in mixed-phase clouds can grow large enough to induce precipitation

529 given sufficient water vapor in the atmosphere. An example is the enhancement of non-convective precipitation over

530 the East China Sea.

531

532 **5 Conclusions**

533 By applying the updated WRF-Chem, which is capable of evaluating indirect effect of dust along with the direct and

534 semi-direct effect in dust simulations, the full effects of dust, including direct radiative, cloud radiative, and indirect

Atmospheric
Chemistry
and Physics
Discussions

Open Access

EGU

535   microphysical effects, on the meteorological field over East Asia during March and April 2012 were quantified and

536   discussed.

537   For the radiative forcing induced by dust, the direct radiative effect of dust combined with the dust-enhanced cloud

538   radiative effect causes a net loss of radiation at the Earth's surface, but a net gain of radiation within the atmosphere,

539   leading to cooling at the surface and lower troposphere, and warming in the mid- to upper troposphere. The radiative

540   forcing caused by the dust-enhanced cloud radiative effect is much greater than that caused by the direct radiative

541   effect of dust, especially for LW radiative forcing, which is highly affected by cloud cover. The LW radiative forcing

542   caused by the dust-enhanced cloud radiative effect is one order stronger than that cased by the direct radiative effect

543   of dust at the top of the atmosphere and within the atmosphere. The spatial distribution of radiative forcing further

544   implies a shift of the spatial distribution of cloud cover, such that the cloud cover is likely increased over land, but

545   reduced over the ocean, due to the presence of dust, indicating a re-distribution of atmospheric water vapor over East

546   Asia.

547   The atmospheric ice water path and ice crystal number density are significantly increased over East Asia, when

548   abundant dust particles are available to serve as ice nuclei. By contrast, the atmospheric cloud water path and cloud

549   droplet number density are substantially reduced. Vertically, the effects of dust result in a general increase of cloud

550   ice and decrease of cloud water over East Asia as a whole, whereby the increase of cloud ice is mainly concentrated

551   at the mid- to upper troposphere, while the decrease in cloud water mostly occurs in low clouds. The increase in clouds

552   at the mid- to upper troposphere is due to the indirect effect of dust by serving as ice nuclei. The reduction in low

553   clouds is attributed to two factors. One is the semi-direct effect of dust. Dust particles within clouds absorb radiation

554   and warm up the surrounding environment, leading to a much greater saturation pressure required for atmospheric

555   water vapor to form clouds, and a much faster evaporation rate of cloud droplets. The other factor is that the ice

556   nucleation process enhanced by dust facilitates the freezing of atmospheric super-cooled water droplets into ice

557   crystals.

558   The radiative forcing and re-distribution of atmospheric water vapor induced by dust lead to a modification of the

559   vertical temperature profile. Consequently, the atmosphere is stabilized over most land areas, but destabilized over

560   most of the ocean in East Asia. The cloud radiative forcing enhanced by dust and the re-distribution of atmospheric

561   water content due to dust contribute much more to the modification of atmospheric stability than the direct radiative

562   effect of dust does.

Atmospheric
Chemistry
and Physics
Discussions

563   Convective precipitation is inhibited over most land areas in East Asia, because of the enhanced atmospheric stability,

564   and the reduction in cloud droplets capable of growing into rain droplets under atmospheric conditions. Conversely,

565   convective precipitation is enhanced over South China and the ocean due to the greater atmospheric instability over

566   these areas. The presence of much fewer cloud droplets in the atmosphere, combined with the atmospheric warming

567   caused by radiative forcing and the release of latent heat by the freezing of super-cooled water droplets, results in a

568   higher saturation pressure for water vapor and faster evaporation rate for cloud droplets, which in turn inhibit non-

569   convective precipitation. The decrease in convective and non-convective precipitation results in a reduction of total

570   precipitation over East Asia. Nevertheless, the increase of cloud ice also leads to more precipitation in some cases.

571   The ice crystals in mixed-phase clouds can grow large enough to induce a precipitation given sufficient atmospheric

572   water vapor.

573

582

Atmospheric
Chemistry
and Physics
Discussions

583 **References**

584 Atkinson, J. D., Murray, B. J., Woodhouse, M. T., Whale, T. F., Baustian, K. J., Carslaw, K. S., Dobbie, S., O'sullivan,

585 D., and Malkin, T. L.: The importance of feldspar for ice nucleation by mineral dust inmixed-phase clouds, Nature,

586 498, 355, 2013.

587 Bi, J., Huang, J., Fu, Q., Ge, J., Shi, J., Zhou, T., and Zhang, W.: Field measurement of clear-sky solar irradiance in

588 Badain Jaran Desert of Northwestern China, Journal of Quantitative Spectroscopy and Radiative Transfer, 122, 194-

589 207, 2013.

590 Chen, Y., Yang, K., He, J., Qin, J., Shi, J., Du, J., and He, Q.: Improving land surface temperature modeling for dry

591 land of China, Journal of Geophysical Research: Atmospheres, 116, 2011.

592 DeMott, P. J., Sassen, K., Poellot, M. R., Baumgardner, D., Rogers, D. C., Brooks, S. D., Prenni, A. J., and Kreidenweis,

593 S. M.: African dust aerosols as atmospheric ice nuclei, Geophysical Research Letters, 30, 2003.

594 DeMott, P. J., Prenni, A. J., McMeeking, G. R., Sullivan, R. C., Petters, M. D., Tobo, Y., Niemand, M., Möhler, O.,

595 Snider, J. R., and Wang, Z.: Integrating laboratory and field data to quantify the immersion freezing ice nucleation

596 activity of mineral dust particles, Atmospheric Chemistry and Physics, 15, 393-409, 2015.

597 Ge, J., Su, J., Ackerman, T., Fu, Q., Huang, J., and Shi, J.: Dust aerosol optical properties retrieval and radiative forcing

598 over northwestern China during the 2008 China-US joint field experiment, Journal of Geophysical Research:

599 Atmospheres, 115, 2010.

600 George, J. J.: Weather forecasting for aeronautics, Academic press, 2014.

601 Ginoux, P., Chin, M., Tegen, I., Prospero, J. M., Holben, B., Dubovik, O., and Lin, S. J.: Sources and distributions of

602 dust aerosols simulated with the GOCART model, Journal of Geophysical Research: Atmospheres, 106, 20255-20273,

603 2001.

604 Ginoux, P., Prospero, J. M., Torres, O., and Chin, M.: Long-term simulation of global dust distribution with the

605 GOCART model: correlation with North Atlantic Oscillation, Environmental Modelling & Software, 19, 113-128,

606 2004.

607 Grell, Ahmadov, R., Peckham, S., Wong, K., Zhang, L., McKeen, S. A., Easter, R., Fast, J. D., Gustafson, W., Ma, P.

608 L., Singh, B., Hodzic, A., Batrth, M., Pfster, G., Wolters, S., Bella, M., Freitas, S. R., Tuccella, P., Zhang, Y., Wang,

609 K., and Klose, M.: WRF-Chem V3. 8: A summary of status and updates, EGU General Assembly Conference Abstracts,

610 2016.

611 Grell, G. A., and Freitas, S. R.: A scale and aerosol aware stochastic convective parameterization for weather and air

612 quality modeling, Atmos. Chem. Phys, 14, 5233-5250, 2014.

613 Hansen, J., Sato, M., and Ruedy, R.: Radiative forcing and climate response, Journal of Geophysical Research:

614 Atmospheres, 102, 6831-6864, 1997.

615 Hartmann, D., Tank, A., and Rusticucci, M.: IPCC fifth assessment report, climate change 2013: The physical science

616 basis, IPCC AR5, 31-39, 2013.

617 Hoose, C., Lohmann, U., Erdin, R., and Tegen, I.: The global influence of dust mineralogical composition on

618 heterogeneous ice nucleation in mixed-phase clouds, Environmental Research Letters, 3, 025003, 2008.

619 Huang, J., Fu, Q., Su, J., Tang, Q., Minnis, P., Hu, Y., Yi, Y., and Zhao, Q.: Taklimakan dust aerosol radiative heating

Atmospheric
Chemistry
and Physics
Discussions

620   derived from CALIPSO observations using the Fu-Liou radiation model with CERES constraints, Atmospheric

621   Chemistry and Physics, 9, 4011-4021, 2009.

622   Huang, J.: Emission, transport, and radiative effects of mineral dust from the Taklimakan and Gobi deserts: comparison

623   of measurements and model results, Atmos. Chem. Phys, 1680, 7324, 2017.

624   Iacono, M. J., Delamere, J. S., Mlawer, E. J., Shephard, M. W., Clough, S. A., and Collins, W. D.: Radiative forcing

625   by long-lived greenhouse gases: Calculations with the AER radiative transfer models, Journal of Geophysical

626   Research: Atmospheres, 113, 2008.

627   Janjić, Z. I.: The step-mountain eta coordinate model: Further developments of the convection, viscous sublayer, and

628   turbulence closure schemes, Monthly Weather Review, 122, 927-945, 1994.

629   Janjić, Z. I.: Nonsingular implementation of the Mellor–Yamada level 2.5 scheme in the NCEP Meso model, NCEP

630   office note, 437, 61, 2002.

631   Karydis, V., Kumar, P., Barahona, D., Sokolik, I., and Nenes, A.: On the effect of dust particles on global cloud

632   condensation nuclei and cloud droplet number, Journal of Geophysical Research: Atmospheres, 116, 2011.

633   Koehler, K., Kreidenweis, S., DeMott, P., Petters, M., Prenni, A., and Möhler, O.: Laboratory investigations of the

634   impact of mineral dust aerosol on cold cloud formation, Atmospheric Chemistry and Physics, 10, 11955-11968, 2010.

635   Lacis, A.: Climate forcing, climate sensitivity, and climate response: A radiative modeling perspective on atmospheric

636   aerosols, Aerosol forcing of climate, 11-42, 1995.

637   Liu, Huang, J., Shi, G., Takamura, T., Khatri, P., Bi, J., Shi, J., Wang, T., Wang, X., and Zhang, B.: Aerosol optical

638   properties and radiative effect determined from sky-radiometer over Loess Plateau of Northwest China, Atmospheric

639   Chemistry and Physics, 11, 11455-11463, 2011a.

640   Liu, Zheng, Y., Li, Z., Flynn, C., Welton, E. J., and Cribb, M.: Transport, vertical structure and radiative properties of

641   dust events in southeast China determined from ground and space sensors, Atmospheric environment, 45, 6469-6480,

642   2011b.

643   Lohmann, U., and Feichter, J.: Global indirect aerosol effects: a review, Atmospheric Chemistry and Physics, 5, 715-

644   737, 2005.

645   Lohmann, U., and Diehl, K.: Sensitivity studies of the importance of dust ice nuclei for the indirect aerosol effect on

646   stratiform mixed-phase clouds, Journal of the Atmospheric Sciences, 63, 968-982, 2006.

647   Mallet, M., Tulet, P., Serça, D., Solmon, F., Dubovik, O., Pelon, J., Pont, V., and Thouron, O.: Impact of dust aerosols

648   on the radiative budget, surface heat fluxes, heating rate profiles and convective activity over West Africa during

649   March 2006, Atmospheric Chemistry and Physics, 9, 7143-7160, 2009.

650   Mlawer, E. J., Taubman, S. J., Brown, P. D., Iacono, M. J., and Clough, S. A.: Radiative transfer for inhomogeneous

651   atmospheres: RRTM, a validated correlated-k model for the longwave, Journal of Geophysical Research: Atmospheres,

652   102, 16663-16682, 1997.

653   Nabat, P., Somot, S., Mallet, M., Michou, M., Sevault, F., Driouech, F., Meloni, D., Di Sarra, A., Di Biagio, C., and

654   Formenti, P.: Dust aerosol radiative effects during summer 2012 simulated with a coupled regional aerosol–

655   atmosphere–ocean model over the Mediterranean, Atmospheric Chemistry and Physics, 15, 3303-3326, 2015a.

656   Nabat, P., Somot, S., Mallet, M., Sevault, F., Chiacchio, M., and Wild, M.: Direct and semi-direct aerosol radiative

657   effect on the Mediterranean climate variability using a coupled regional climate system model, Climate dynamics, 44,

658   1127-1155, 2015b.

659   Palacios, L., Baró, R., and Jiménez-Guerrero, P.: An on-line modelling study of the direct effect of atmospheric

660   aerosols over Europe, Física de la Tierra, 27, 155, 2015.

661   Perlwitz, J., and Miller, R. L.: Cloud cover increase with increasing aerosol absorptivity: A counterexample to the

662   conventional semidirect aerosol effect, Journal of Geophysical Research: Atmospheres, 115, 2010.

663   Pinker, R., and Laszlo, I.: Modeling surface solar irradiance for satellite applications on a global scale, Journal of

664   Applied Meteorology, 31, 194-211, 1992.

665   Rodell, M., Houser, P., Jambor, U., Gottschalck, J., Mitchell, K., Meng, C., Arsenault, K., Cosgrove, B., Radakovich,

666   J., and Bosilovich, M.: The global land data assimilation system, Bulletin of the American Meteorological Society, 85,

667   381-394, 2004.

668   Sassen, K., DeMott, P. J., Prospero, J. M., and Poellot, M. R.: Saharan dust storms and indirect aerosol effects on

669   clouds: CRYSTAL-FACE results, Geophysical Research Letters, 30, 2003.

670   Satheesh, S., Deepshikha, S., and Srinivasan, J.: Impact of dust aerosols on Earth–atmosphere clear-sky albedo and

671   its short wave radiative forcing over African and Arabian regions, International Journal of Remote Sensing, 27, 1691-

672   1706, 2006.

673   Seigel, R., Van Den Heever, S., and Saleeby, S.: Mineral dust indirect effects and cloud radiative feedbacks of a

674   simulated idealized nocturnal squall line, Atmospheric Chemistry and Physics, 13, 4467-4485, 2013.

675   Seinfeld, J. H., Carmichael, G. R., Arimoto, R., Conant, W. C., Brechtel, F. J., Bates, T. S., Cahill, T. A., Clarke, A. D.,

676   Doherty, S. J., and Flatau, P. J.: ACE-ASIA: Regional climatic and atmospheric chemical effects of Asian dust and

677   pollution, Bulletin of the American Meteorological Society, 85, 367-380, 2004.

678   Sheffield, J., Goteti, G., and Wood, E. F.: Development of a 50-year high-resolution global dataset of meteorological

679   forcings for land surface modeling, Journal of Climate, 19, 3088-3111, 2006.

680   Solomon, S.: Climate change 2007-the physical science basis: Working group I contribution to the fourth assessment

681   report of the IPCC, Cambridge University Press, 2007.

682   Targino, A. C., Krejci, R., Noone, K. J., and Glantz, P.: Single particle analysis of ice crystal residuals observed in

683   orographic wave clouds over Scandinavia during INTACC experiment, Atmospheric Chemistry and Physics, 6, 1977-

684   1990, 2006.

685   Teller, A., and Levin, Z.: The effects of aerosols on precipitation and dimensions of subtropical clouds: a sensitivity

686   study using a numerical cloud model, Atmospheric Chemistry and Physics, 6, 67-80, 2006.

687   Tesfaye, M., Tsidu, G. M., Botai, J., and Sivakumar, V.: Mineral dust aerosol distributions, its direct and semi-direct

688   effects over South Africa based on regional climate model simulation, Journal of Arid Environments, 114, 22-40, 2015.

689   Wesely, M.: Parameterization of surface resistances to gaseous dry deposition in regional-scale numerical models,

690   Atmospheric Environment (1967), 23, 1293-1304, 1989.

691   Yang, K., He, J., Tang, W., Qin, J., and Cheng, C. C.: On downward shortwave and longwave radiations over high

692   altitude regions: Observation and modeling in the Tibetan Plateau, Agricultural and Forest Meteorology, 150, 38-46,

693   2010.

694 Zhang, C., Wang, M., Morrison, H., Somerville, R. C., Zhang, K., Liu, X., and Li, J. L. F.: Investigating ice nucleation

695 in cirrus clouds with an aerosol-enabled Multiscale Modeling Framework, Journal of Advances in Modeling Earth

696 Systems, 6, 998-1015, 2014.

697

698

Atmospheric
Chemistry
and Physics
Discussions

Open Access

EGU

699 **List of tables and figures**

700 Table 1: Model configurations for the numerical simulations.

701 Table 2: WRF-Chem-simulated SW, LW, and net radiative forcing (W/m^2) induced by dust over East Asia at TOA,

702 BOT, and ATM.

703 Figure 1: Spatial distributions of the average downward SW radiation at surface from observations (a, b), from NO-

704 AER/CLOUD (c, d), and from AER-CLOUD (e, f) during March (left panel) and April (right panel) 2012.

705 Figure 2: Spatial distributions of the average downward LW radiation at surface from observations (a, b), from NO-

706 AER/CLOUD (c, d), and from AER-CLOUD (e, f) during March (left panel) and April (right panel) 2012.

707 Figure 3: Spatial distributions of the average near-surface temperature from observations (a, b), from NO-

708 AER/CLOUD (c, d), and from AER-CLOUD (e, f) during March (left panel) and April (right panel) 2012.

709 Figure 4: Spatial distributions of the average precipitation rate from observations (a, b), from NO-AER/CLOUD (c,

710 d), and from AER-CLOUD (e, f) during March (left panel) and April (right panel) 2012.

711 Figure 5: Spatial distributions of the clear-sky SW (left panel), LW (middle panel), and net (right panel) radiative

712 forcing at the top of the atmosphere (TOA, a-c), within the atmosphere (ATM, d-f), and at the bottom of the atmosphere

713 (BOT, g-i).

714 Figure 6: Spatial distributions of the all-sky SW (left panel), LW (middle panel), and net (right panel) radiative forcing

715 at the top of the atmosphere (TOA, a-c), within the atmosphere (ATM, d-f), and at the bottom of the atmosphere (BOT,

716 g-i).

717 Figure 7: Spatial distributions of the average simulated precipitable water vapor (a-c), ice water path (d-f), and cloud

718 water path (g-i) from NO-AER/CLOUD (left panel), AER/CLOUD (middle panel), and difference between

719 AER/CLOUD and NO-AER/CLOUD (right panel).

720 Figure 8: Spatial distributions of the average simulated ice crystal number density (a-c) and cloud droplet number

721 density (d-f) from NO-AER/CLOUD (left panel), AER/CLOUD (middle panel), and difference between

722 AER/CLOUD and NO-AER/NO-CLOUD (right panel).

723 Figure 9: Vertical profile of the modification of cloud ice (a-c) and cloud water content (e-f) induced by dust over the

724 entire simulation domain (left panel), over land (middle panel), and over ocean (right panel).

725 Figure 10: Modification of vertical temperature profile induced by the full effects of dust (left panel), the direct

726 radiative effect of dust (middle panel), and the semi-direct and indirect effects of dust (right panel) over the entire

Atmospheric
Chemistry
and Physics
Discussions

727   simulation domain (a-c), over land (d-f), and over ocean (g-i).

728   Figure 11: Spatial distributions of the monthly average K-index from NO-AER/CLOUD.

729   Figure 12: Spatial distributions of the modification of K-index induced by the direct radiative effect of dust (a), the

730   semi-direct and indirect effects of dust (b), and the full effects of dust (c).

731   Figure 13: Spatial distributions of the average simulated total precipitation rate (a-c), convective precipitation rate (d-

732   f), and non-convective precipitation rate (g-i) from NO-AER/CLOUD (left panel), AER/CLOUD (middle panel), and

733   the difference between AER/CLOUD and NO-AER/CLOUD (right panel).

734

Atmospheric
Chemistry
and Physics
Discussions

735   **Table 1:** Model configurations for the numerical simulations.

Experiment / Scheme	NO-AER/NO-CLOUD	NO-AER/CLOUD	AER/NO-CLOUD	AER/CLOUD
Dust emission scheme	----	----	Shao	Shao
Soil dataset	USGS	USGS	USGS	USGS
Land surface model	Noah LSM	Noah LSM	Noah LSM	Noah LSM
Planetary boundary layer	MYJ	MYJ	MYJ	MYJ
Moisture convection	Grell–Freitas	Grell–Freitas	Grell–Freitas	Grell–Freitas
Long-wave radiation	RRTMG	RRTMG	RRTMG	RRTMG
Short-wave radiation	RRTMG	RRTMG	RRTMG	RRTMG
Microphysics	GOCART-Thompson	GOCART-Thompson	GOCART-Thompson	GOCART-Thompson
Chemistry mechanism	GOCART	GOCART	GOCART	GOCART
Dry deposition	----	----	Gravitational settling/surface deposition	Gravitational settling/surface deposition
Wet deposition	----	----	In-cloud and below-cloud	In-cloud and below-cloud
Aerosol optical scheme	----	----	Maxwell-Garnett	Maxwell-Garnett
Aerosol radiative feedback	off	off	on	on
Cloud radiative feedback	off	on	off	on

736

Table 2: WRF-Chem-simulated SW, LW, and net radiative forcing (W/m^2) induced by dust over East Asia at TOA, BOT, and ATM.

	Clear-sky			All-sky		
	SW	LW	Net	SW	LW	Net
TOA (+down)	-1.22	0.02	-1.20	-7.81	9.52	1.70
ATM (+warm)	1.23	-1.07	0.15	0.06	9.26	9.33
BOT (+down)	-2.44	1.09	-1.36	-7.87	0.25	-7.62

SW: short-wave radiative forcing; LW: long-wave radiative forcing; Net: net radiative forcing.
TOA: radiative forcing at the top of the atmosphere; ATM: radiative effect within the atmosphere; BOT: radiative effect at the bottom of the atmosphere.
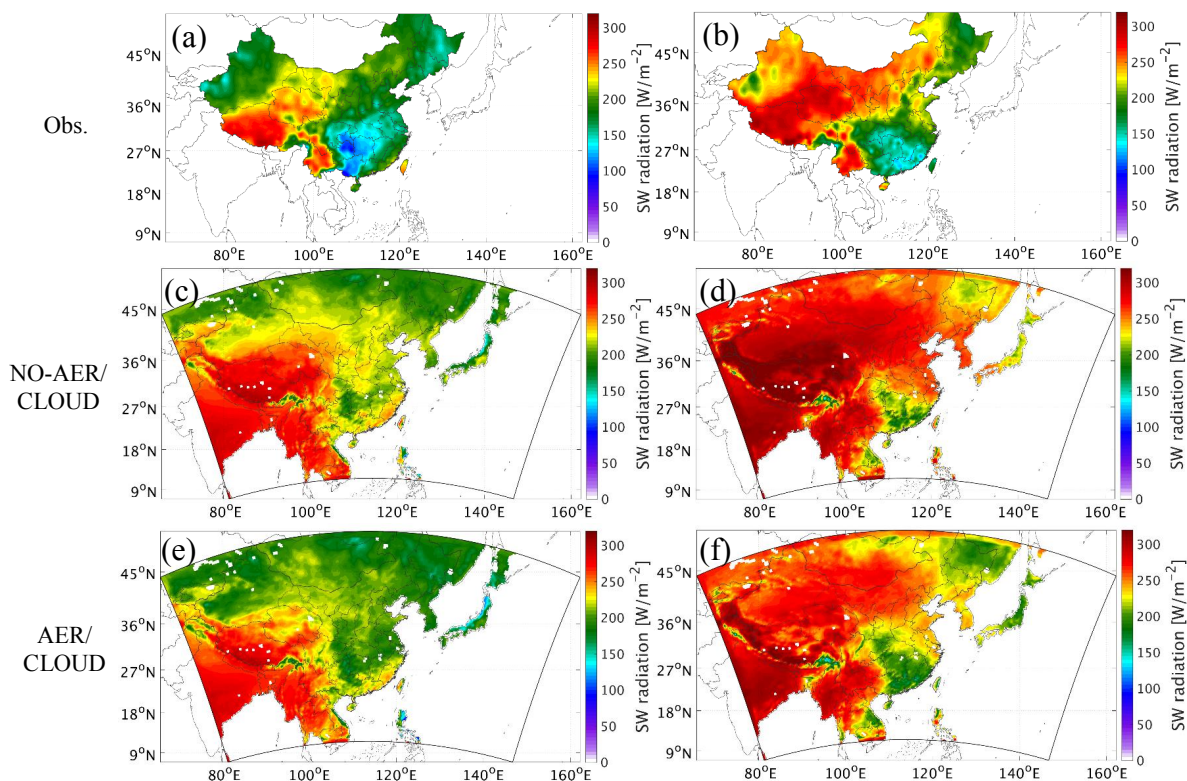
Figure 1: Spatial distributions of the average downward SW radiation at surface from observations (a, b), from NO-AER/CLOUD (c, d), and from AER-CLOUD (e, f) during March (left panel) and April (right panel) 2012.
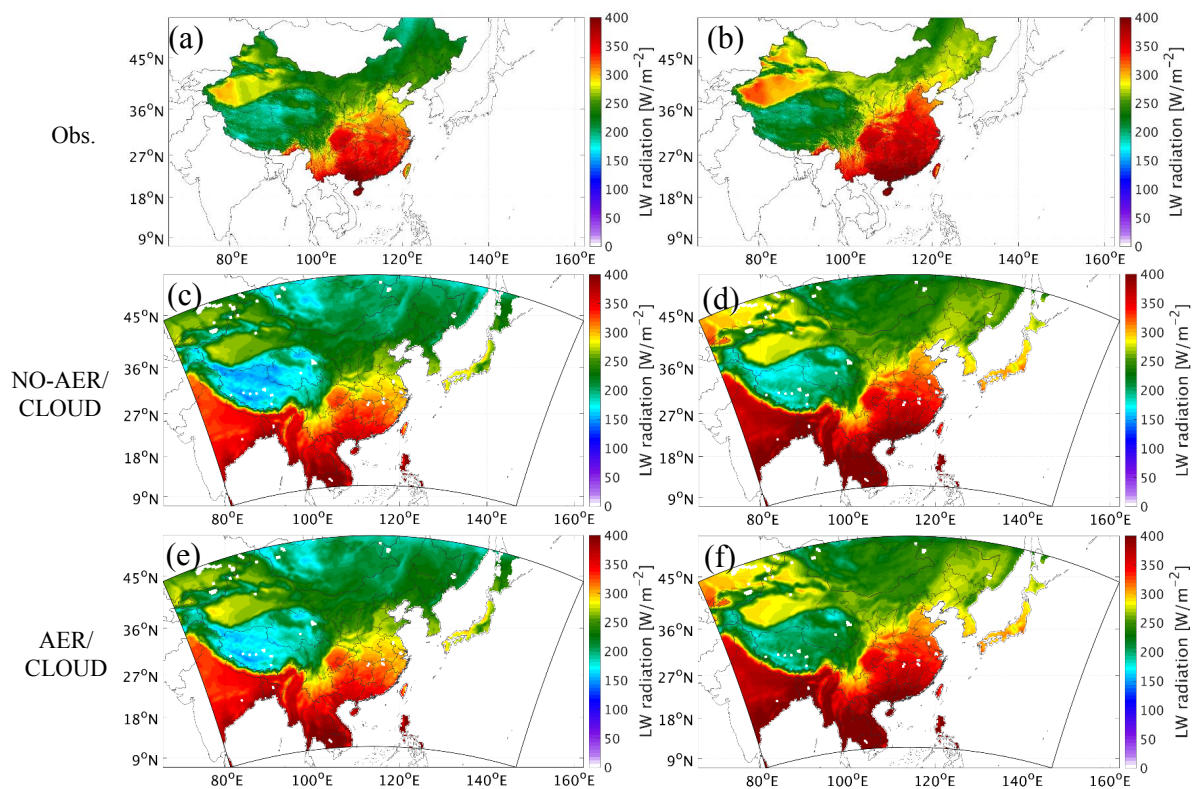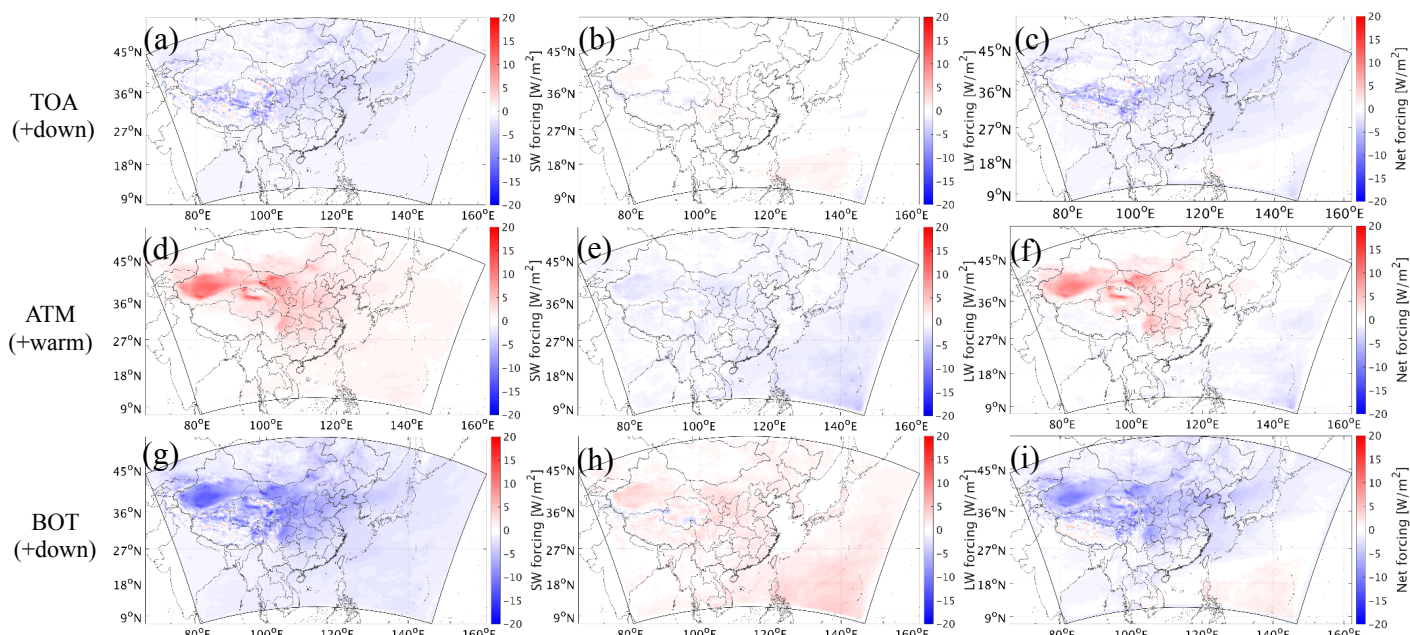
Figure 2: Spatial distributions of the average downward LW radiation at surface from observations (a, b), from NO-AER/CLOUD (c, d), and from AER-CLOUD (e, f) during March (left panel) and April (right panel) 2012.

Figure 3: Spatial distributions of the average near-surface temperature from observations (a, b), from NO-AER/CLOUD (c, d), and from AER-CLOUD (e, f) during March (left panel) and April (right panel) 2012.

Atmospheric
Chemistry
and Physics
Discussions
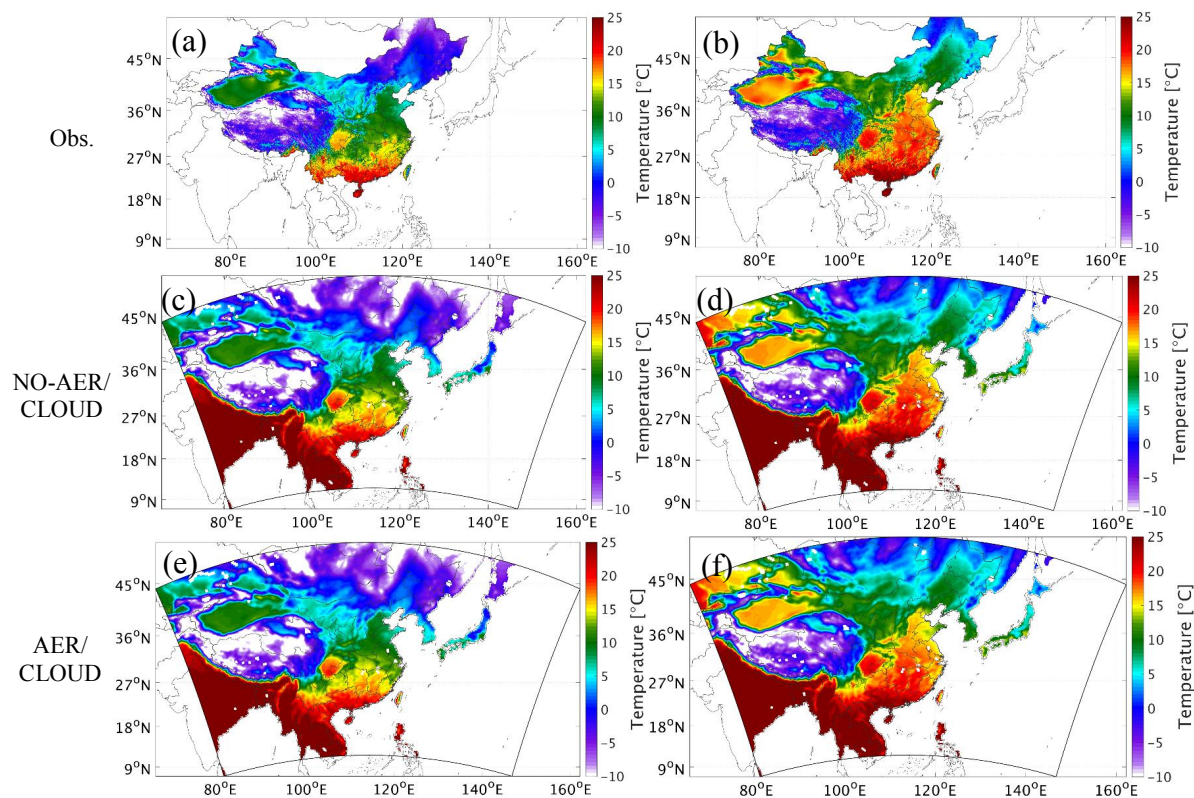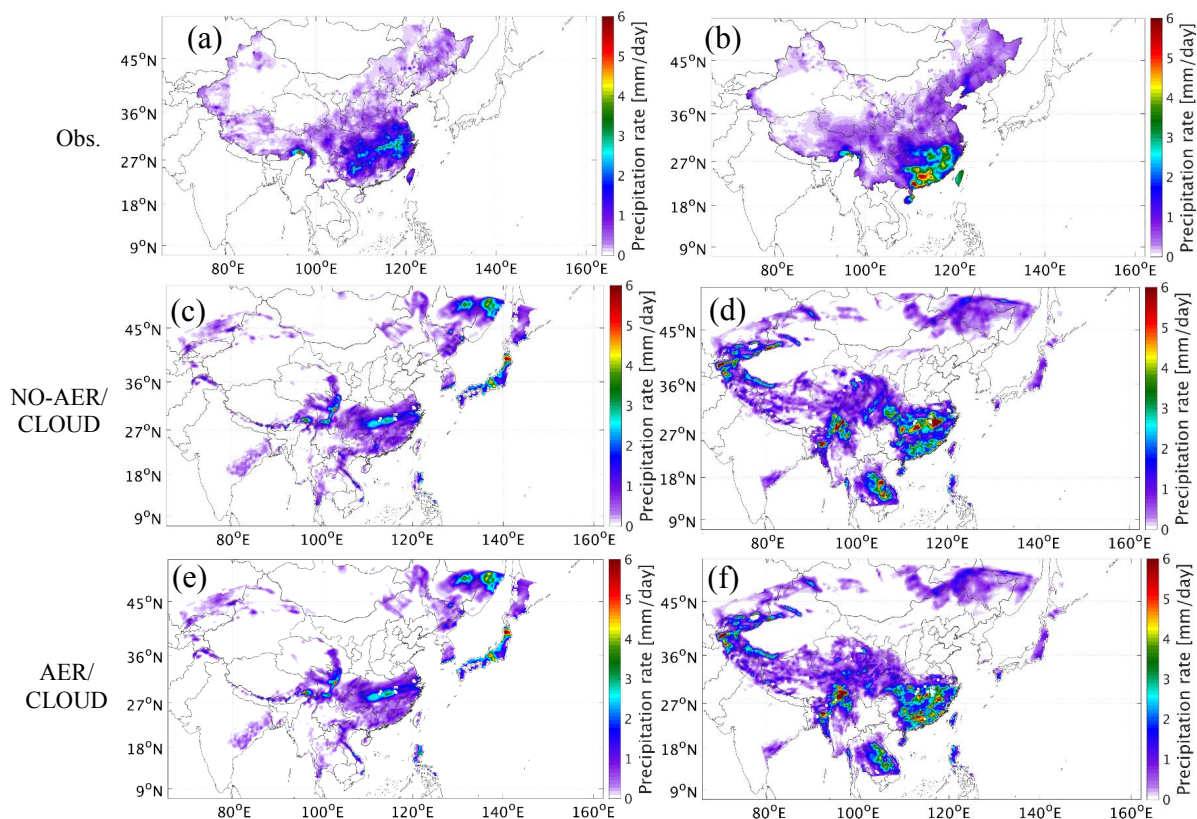
Figure 4: Spatial distributions of the average precipitation rate from observations (a, b), from NO-AER/CLOUD (c, d), and from AER/CLOUD (e, f) during March (left panel) and April (right panel) 2012.

SW   LW   Net

Atmospheric
Chemistry
and Physics
Discussions
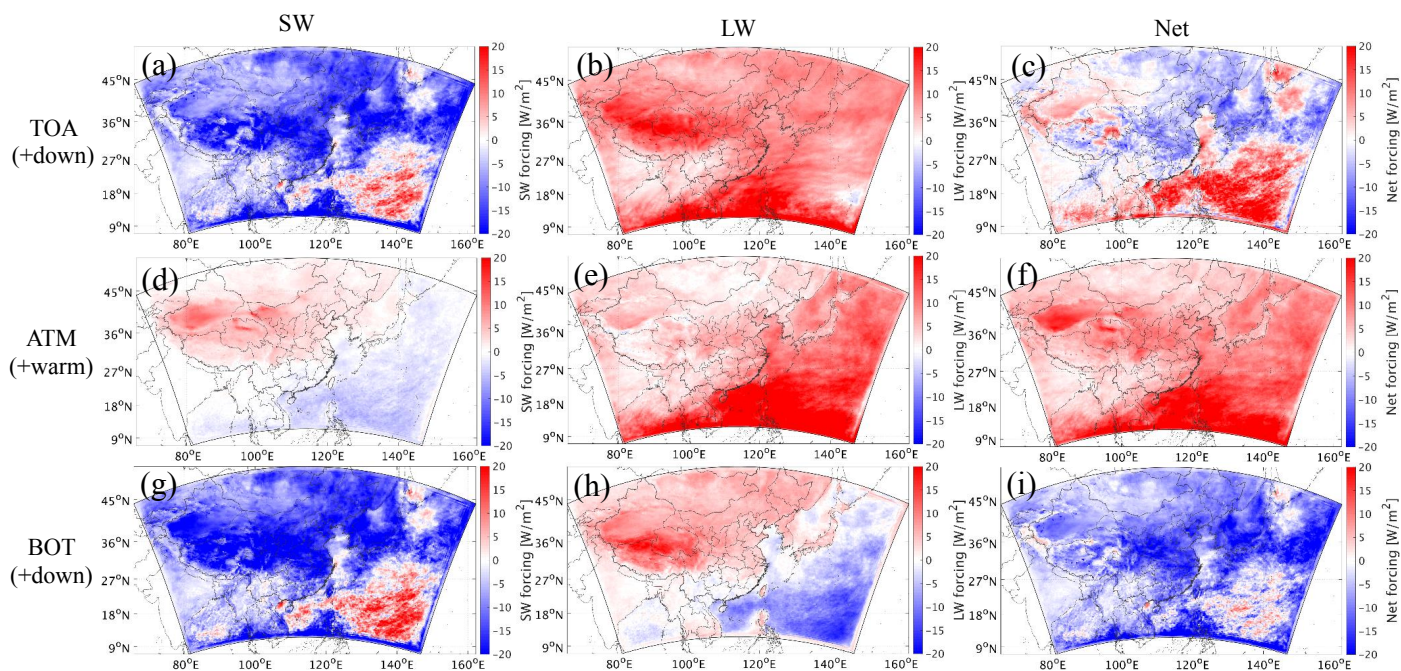
Figure 5: Spatial distributions of the clear-sky SW (left panel), LW (middle panel), and net (right panel) radiative forcing at the top of the atmosphere (TOA, a-c), within the atmosphere (ATM, d-f), and at the bottom of the atmosphere (BOT, g-i).

Figure 6: Spatial distributions of the all-sky SW (left panel), LW (middle panel), and net (right panel) radiative forcing at the top of the atmosphere (TOA, a-c), within the atmosphere (ATM, d-f), and at the bottom of the atmosphere (BOT, g-i).

Atmospheric
Chemistry
and Physics
Discussions
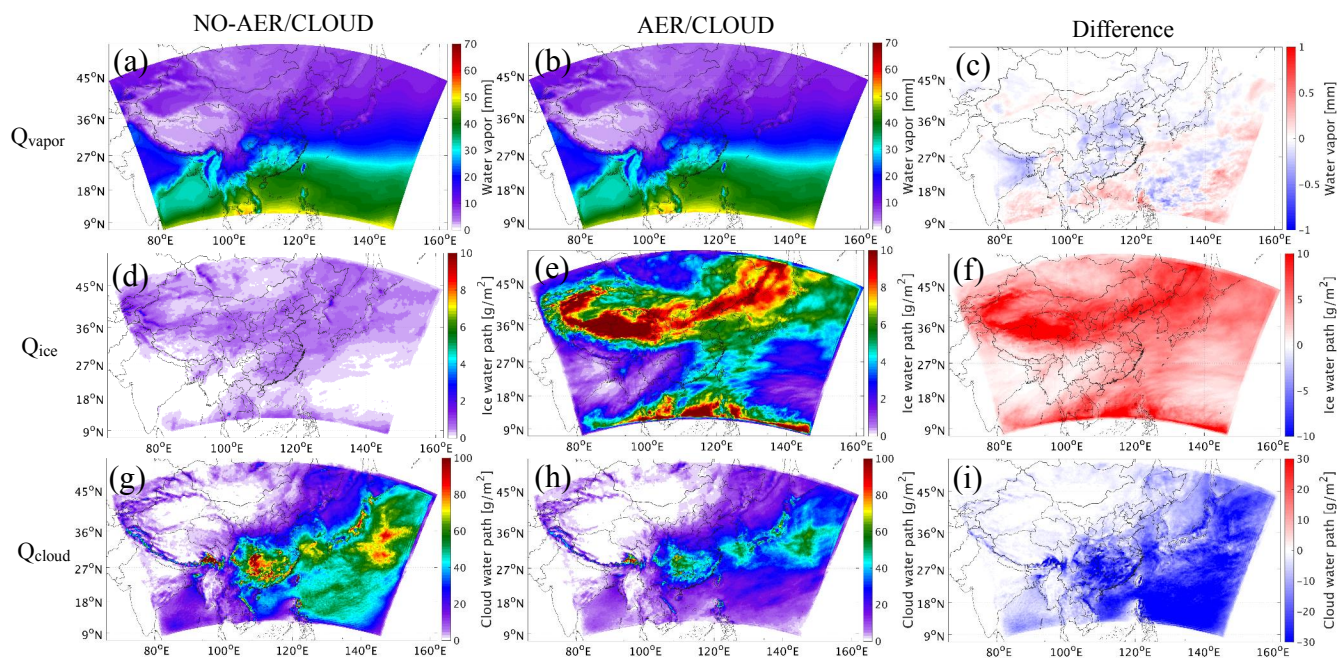
Figure 7: Spatial distributions of the average simulated precipitable water vapor (a-c), ice water path (d-f), and cloud water path (g-i) from NO-AER/CLOUD (left panel), AER/CLOUD (middle panel), and difference between AER/CLOUD and NO-AER/CLOUD (right panel).
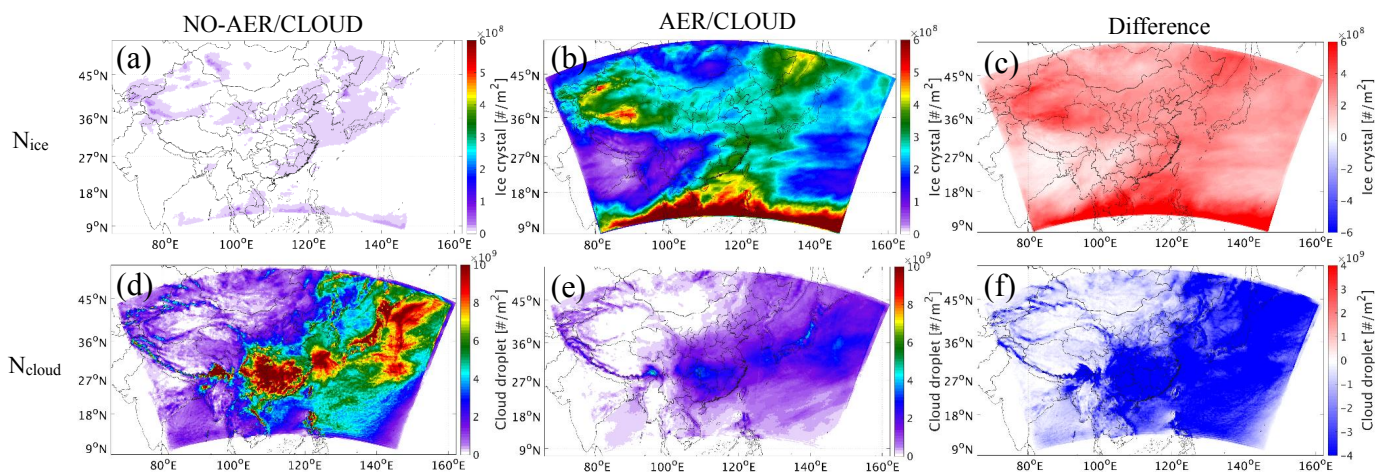
Figure 8: Spatial distributions of the average simulated ice crystal number density (a-c) and cloud droplet number density (d-f) from NO-AER/CLOUD (left panel), AER/CLOUD (middle panel), and difference between AER/CLOUD and NO-AER/NO-CLOUD (right panel).
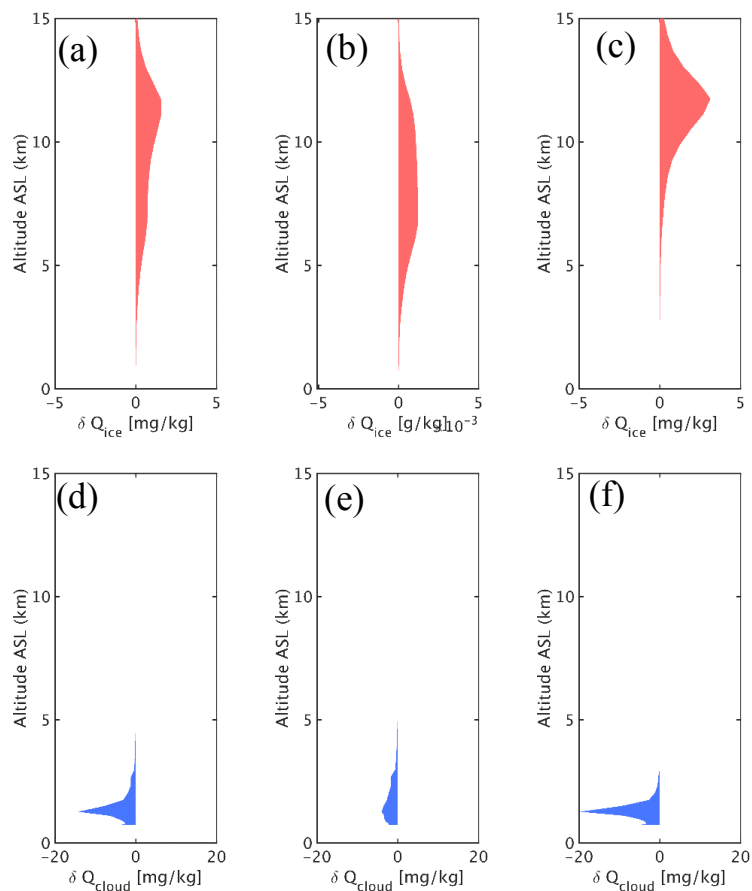
Figure 9: Vertical profile of the modification of cloud ice (a-c) and cloud water content (e-f) induced by dust over the entire simulation domain (left panel), over land (middle panel), and over ocean (right panel).
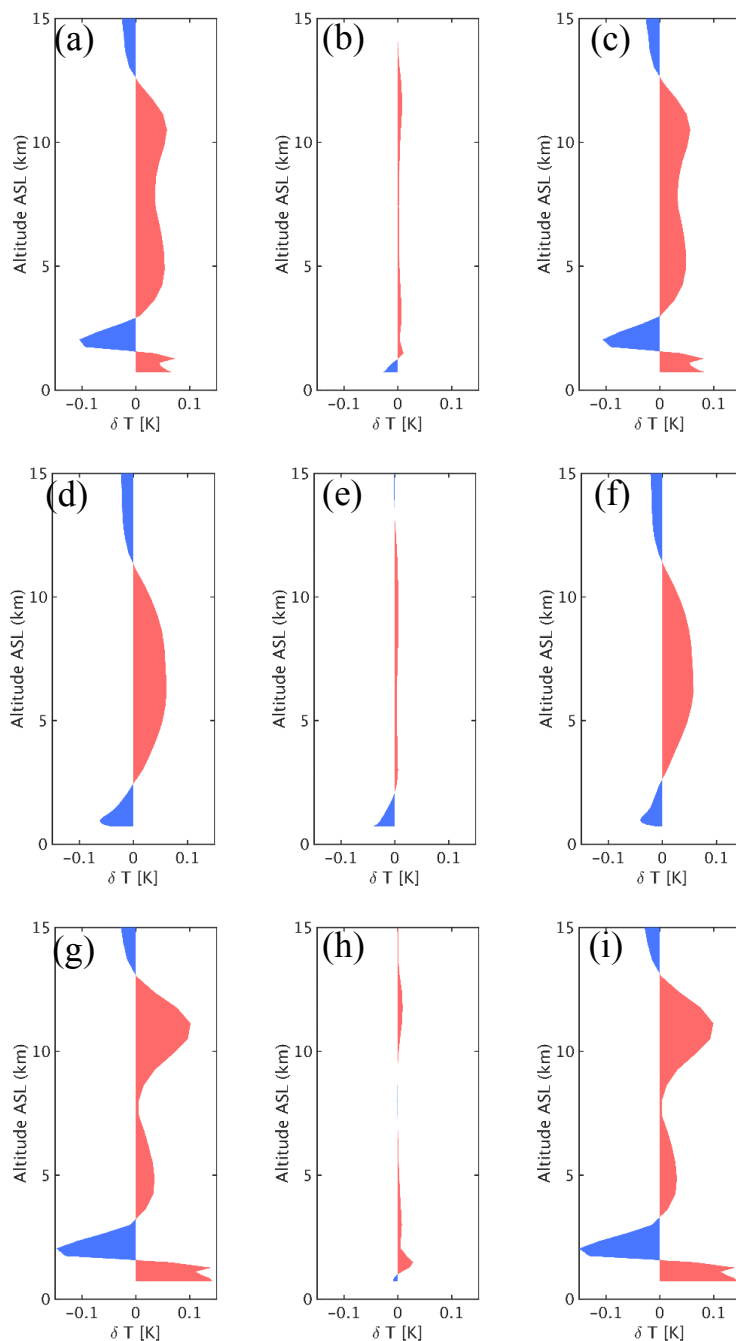
Figure 10: Modification of vertical temperature profile induced by the full effects of dust (left panel), the direct radiative effect of dust (middle panel), and the semi-direct and indirect effects of dust (right panel) over the entire simulation domain (a-c), over land (d-f), and over ocean (g-i).
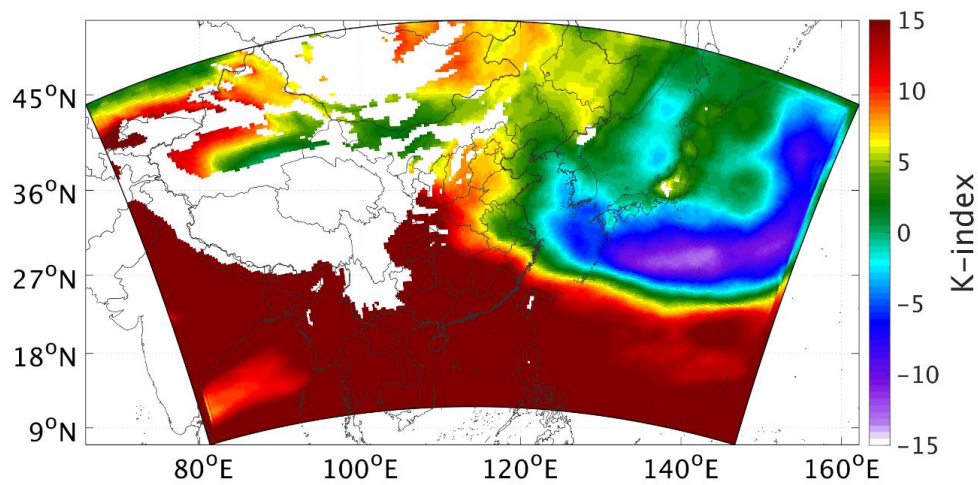
Figure 11: Spatial distributions of the monthly average K-index from NO-AER/CLOUD.
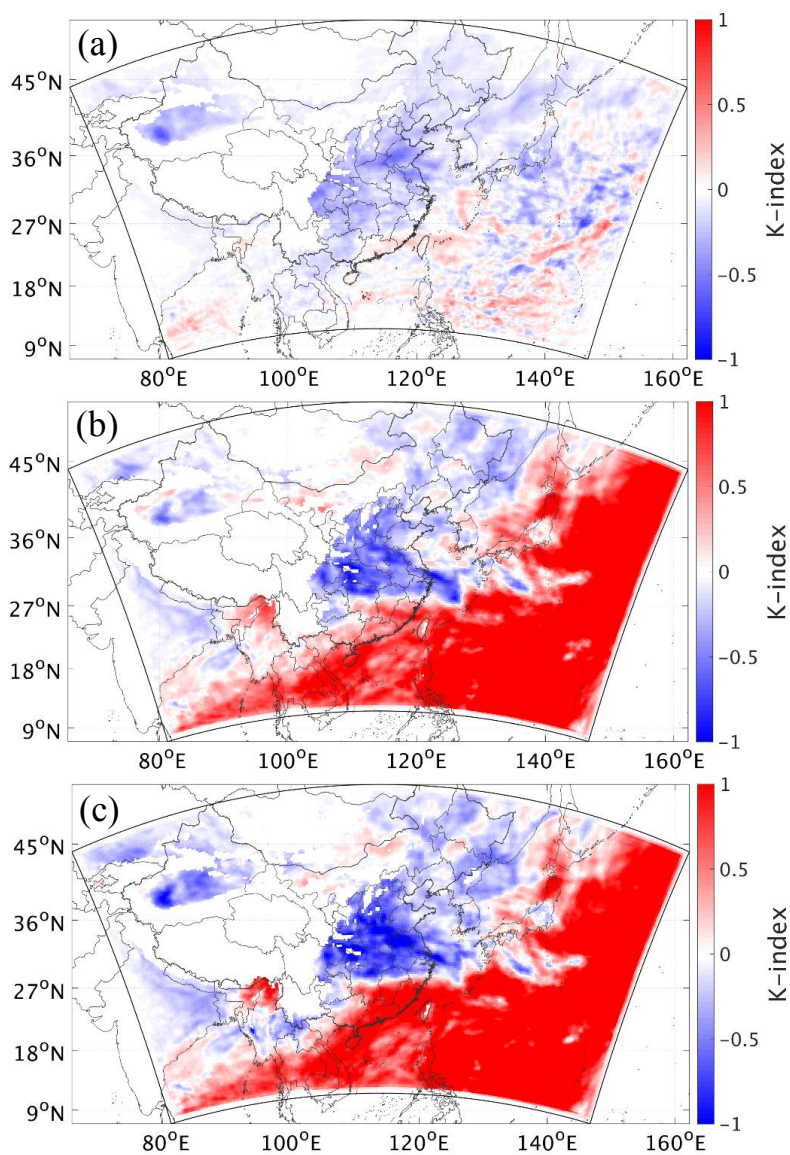
Figure 12: Spatial distributions of the modification of K-index induced by the direct radiative effect of dust (a), the semi-direct and indirect effects of dust (b), and the full effects of dust (c).
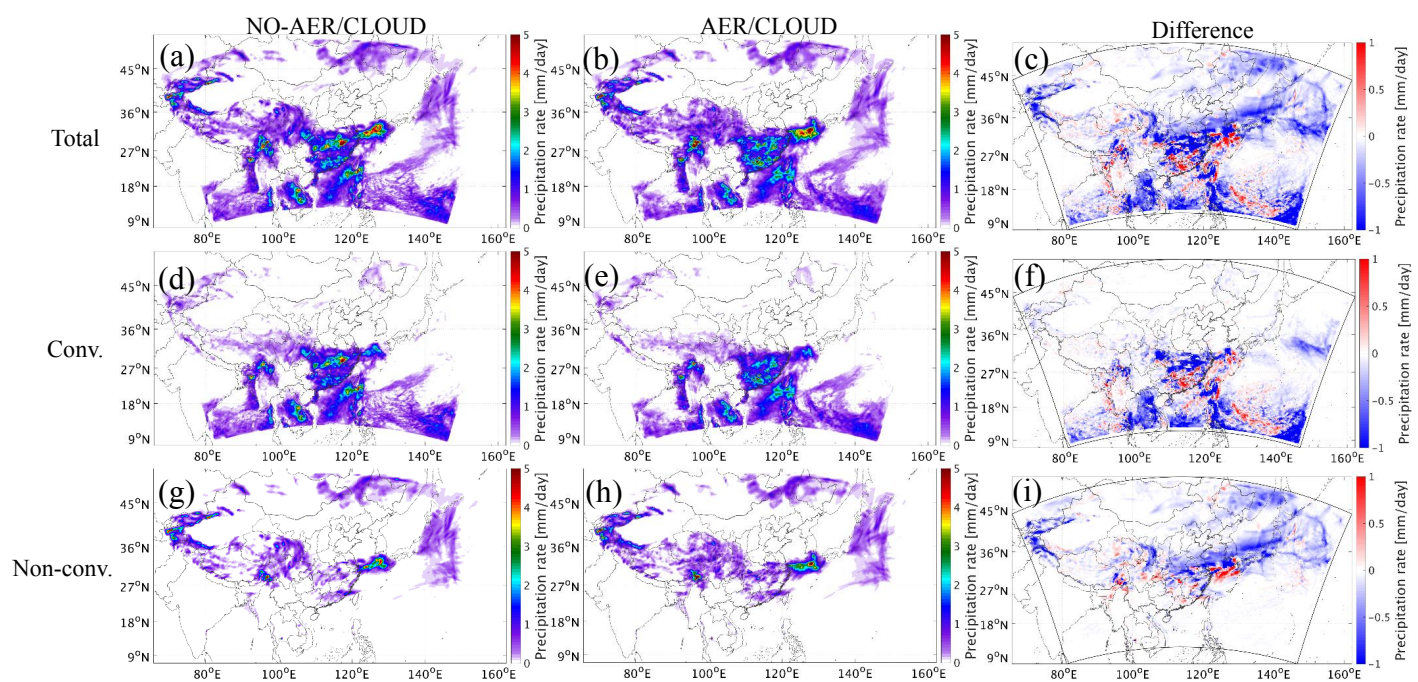
Figure 13: Spatial distributions of the average simulated total precipitation rate (a-c), convective precipitation rate (d-f), and non-convective precipitation rate (g-i) from NO-AER/CLOUD (left panel), AER/CLOUD (middle panel), and the difference between AER/CLOUD and NO-AER/CLOUD (right panel).